Mechie, J., Abu-Ayyash, K., Ben-Avraham, Z., El-Kelani, R., Qabbani, I., Weber, M., DESIRE Team (2009): Crustal structure of the southern Dead Sea basin derived from project DESIRE wide-angle seismic data. - Geophysical Journal International, 178, 1, pp. 457—478.

DOI: http://doi.org/10.1111/j.1365-246X.2009.04161.x

Geophys. J. Int. (2009) **178,** 457–478 doi: 10.1111/j.1365-246X.2009.04161.x

Crustal structure of the southern Dead Sea basin derived from project DESIRE wide-angle seismic data

J. Mechie,[1] K. Abu-Ayyash,[1,2] Z. Ben-Avraham,[3] R. El-Kelani,[4] I. Qabbani,[2] M. Weber[1,5] and DESIRE Group

[1]*Deutsches GeoForschungsZentrum—GFZ, Section 'Geophysical Deep Sounding', Telegrafenberg,* 14473 *Potsdam, Germany. E-mail: jimmy@gfz-potsdam.de*
[2]*Natural Resources Authority, Amman, Jordan*
[3]*Department of Geophysics and Planetary Sciences, Tel-Aviv University, Tel-Aviv, Israel*
[4]*An-Najah National University, Nablus, Palestine*
[5]*Institut für Geowissenschaften, Universität Potsdam, Potsdam, Germany*

Accepted 2009 February 14. Received 2009 February 14; in original form 2008 February 25

SUMMARY

As part of the DEad Sea Integrated REsearch project (DESIRE) a 235 km long seismic wide-angle reflection/refraction (WRR) profile was completed in spring 2006 across the Dead Sea Transform (DST) in the region of the southern Dead Sea basin (DSB). The DST with a total of about 107 km multi-stage left-lateral shear since about 18 Ma ago, accommodates the movement between the Arabian and African plates. It connects the spreading centre in the Red Sea with the Taurus collision zone in Turkey over a length of about 1 100 km. With a sedimentary infill of about 10 km in places, the southern DSB is the largest pull-apart basin along the DST and one of the largest pull-apart basins on Earth. The WRR measurements comprised 11 shots recorded by 200 three-component and 400 one-component instruments spaced 300 m to 1.2 km apart along the whole length of the E–W trending profile. Models of the *P*-wave velocity structure derived from the WRR data show that the sedimentary infill associated with the formation of the southern DSB is about 8.5 km thick beneath the profile. With around an additional 2 km of older sediments, the depth to the seismic basement beneath the southern DSB is about 11 km below sea level beneath the profile. Seismic refraction data from an earlier experiment suggest that the seismic basement continues to deepen to a maximum depth of about 14 km, about 10 km south of the DESIRE profile. In contrast, the interfaces below about 20 km depth, including the top of the lower crust and the Moho, probably show less than 3 km variation in depth beneath the profile as it crosses the southern DSB. Thus the Dead Sea pull-apart basin may be essentially an upper crustal feature with upper crustal extension associated with the left-lateral motion along the DST. The boundary between the upper and lower crust at about 20 km depth might act as a decoupling zone. Below this boundary the two plates move past each other in what is essentially a shearing motion. Thermo-mechanical modelling of the DSB supports such a scenario. As the DESIRE seismic profile crosses the DST about 100 km north of where the DESERT seismic profile crosses the DST, it has been possible to construct a crustal cross-section of the region before the 107 km left-lateral shear on the DST occurred.

Key words: Controlled source seismology; Transform faults.

INTRODUCTION

The Dead Sea Transform (DST) forms the boundary between the African and Arabian plates at the northwestern flank of the Nubo-Arabian Shield (Fig. 1). It trends N-NNE for about 1 100 km from the northern Red Sea in the south to the collision zone at the Taurus mountains in the north. Since its inception about 18 Ma ago it has accommodated about 107 km of left-lateral movement between the two plates (Quennell 1958; Freund *et al*. 1970; Garfunkel 1981, 1997). Along its southern portion huge pull-apart basins, for example the Dead Sea basin (DSB), Gulf of Aqaba/Elat, alternate with strands of strike-slip dominated, relatively simple shear zones, for example the Arava/Araba valley. The DSB is the largest pull-apart basin along the DST and one of the largest such features on Earth.

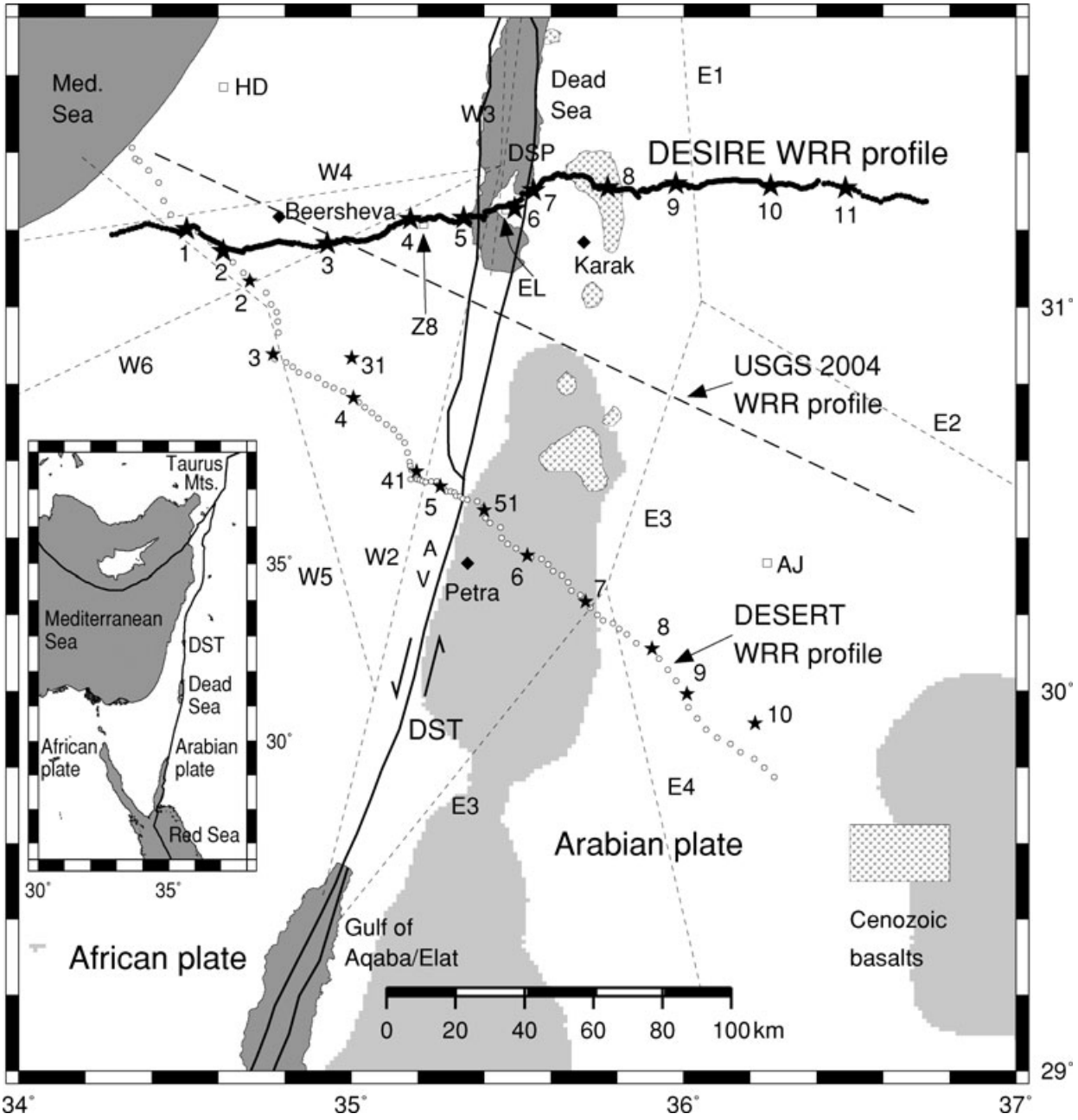

Figure 1. Location map for the 235 km long DESIRE wide-angle reflection/refraction (WRR) profile crossing the DST in the region of the southern DSB. During the WRR experiment, 11 shots (large stars with numbers) were executed and recorded by 200 three-component and 400 one-component instruments (circles) spaced 300 m to 1.2 km apart along the whole length of the profile. The shots (small stars with numbers) and the three-component sites (unfilled circles) of the DESERT WRR experiment, completed in 2000, are also shown as is the position of the USGS profile (thick dashed line) which crossed the DST and was carried out in 2004. Previous profiles E1–E4 (El-Isa *et al*. 1987a, b), W2–W6 (Ginzburg *et al*. 1979a, b) and DSP (Ginzburg & Ben-Avraham 1997) are also shown as thin dashed lines. The main strands of the DST and the Cenozoic volcanics are after Garfunkel (1997). Ground above 1 000 m is shaded light grey, while areas of water are shaded dark grey. The positions of the Helez-Deep-1A (HD), Zohar-8 deep (Z8), El Lisan 1 (EL) and Al Jafr (AJ) boreholes are also marked. *Key*: AV: Arava/Araba valley. The inset shows the regional tectonic setting of the DST.

In its southern part the Cenozoic basin fill has been estimated to have a thickness in excess of 8 km and the Precambrian crystalline basement has been estimated to occur at about 14 km depth in some places (Ginzburg & Ben-Avraham 1997; Ben-Avraham & Schubert 2006).

The main goal of the seismic wide-angle reflection/refraction (WRR) profile described here was to determine the *P*- and *S*-wave velocity structure beneath the southern DSB, in an attempt to distinguish between the various models, which have been proposed for the formation of the DSB. Specifically, it was aimed at determining the thickness of the basin and the topography of the crust–mantle boundary (Moho) and the top of the lower crust beneath the profile, in order to estimate the amount of crustal thinning and how this thinning is distributed in the crust beneath the DSB. Together with the two other seismic WRR profiles which now exist across the DST (Fig. 1), the amount and depth distribution of extension

both along and across the DSB can be examined. The amount and depth distribution of extension are criteria, which can be used to distinguish between the various models for the formation of the DSB.

The morphology of the Dead Sea/Araba valley is very similar to that of a classical rift valley with a topographic depression in the valley and steep-sided shoulders on both sides of the valley. For example, where the DEad Sea Integrated REsearch project (DESIRE) profile crossed the DSB, the topographic difference on the west side of the valley is 1 000 m and on the east side of the valley it is 1 300 m. The main difference between the Dead Sea/Araba valley and most other rift valleys is that the Dead Sea/Araba valley is somewhat narrower. For example, where the DESIRE profile crossed the DSB the valley is only 17 km wide. This is in contrast to, for example the southern Kenya rift which is 50–70 km wide at its narrowest point and the Rhinegraben which is generally about 40 km wide. Nevertheless, the Dead Sea/Araba valley has often been thought of as a rift structure and many publications include the word 'rift' in the title (e.g. Quennell 1958; Ginzburg *et al.* 1979a,b). Implicit in this model is the idea of E–W extension (Fig. 2a). However, early on, it has also been recognized that a significant amount of strike-slip motion has occurred along the structure (Fig. 2b) and Quennell (1958) put a figure of about 107 km of left-lateral strike-slip motion. With the recognition of the significant amount of strike-slip motion along the DST came also the realisation that the DSB was not formed just by E–W extension but was a pull-apart basin, formed due to the side-stepping of the main strike-slip motion from the east side of the valley at the southern end of the basin to the west side of the valley north of the basin (e.g. Garfunkel 1981; ten Brink *et al.* 1993; Garfunkel & Ben-Avraham 1996). Thus, Garfunkel (1981) coined the term 'leaky transform' to indicate E–W extension in addition to pull-apart basin formation. Implicit in the model of a significant pull-apart component for the origin of the DSB is the idea of N–S extension (Fig. 2c) and ten Brink *et al.* (1993) showed a model with extension in the N–S direction but without any Moho uplift (Fig. 2d). Later Al-Zoubi & ten Brink (2002) proposed that lower crustal channel flow from the southern to the central part of the DSB might be occurring due to extension of the upper crust beneath the central part of the DSB and distributed lower crustal thinning (Fig. 2e). Subsequent thermo-mechanical modelling of the structure using the finite-element method and what was known from geology and geophysics about the structure has been carried out by Sobolev *et al.* (2005) and Petrunin & Sobolev (2006). In particular, Petrunin & Sobolev (2006) predicted that Moho uplift beneath the southern DSB is less than 3 km. Alternative models for the formation of the DSB include that in which E–W extension accompanies strike-slip motion (Figs 2a and b) but without the need for a pull-apart component (Ben-Avraham & Zoback 1992). Finally, Ben-Avraham & Schubert (2006) put forward a drop-down model for the southern DSB in which the whole lithosphere beneath the southern DSB is dropped down with respect to the surrounding regions, due to the great thickness of sediments in the southern DSB (Fig. 2f). Ben-Avraham & Schubert (2006) also proposed such a model for the Salton Trough, the deepest basin along the San Andreas fault system. Previously, Fuis *et al.* (1984) had described the Salton Trough as a rift with fault-perpendicular extension. With the existence now of three WRR profiles across the DST in the southern DSB and Araba valley, there is the chance to distinguish between the various models proposed for the formation of the structure and, in particular, whether extension is uniform throughout the whole crust or is partitioned with, for example more extension occurring in the upper crust than in the lower crust.

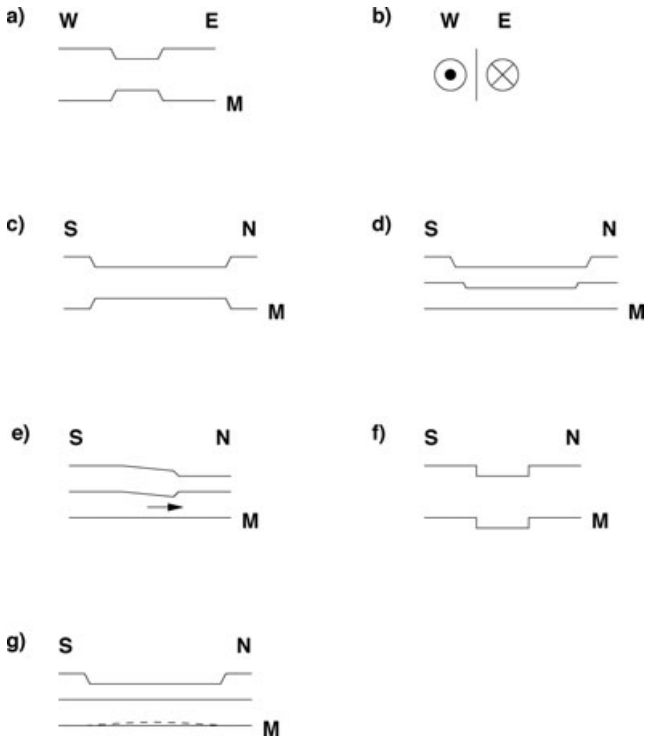

Figure 2. Simplified cross-sections of basic structural elements used in models for the DSB. (a) whole-crustal E–W extension (rift), (b) left-lateral strike-slip motion, (c) whole-crustal N–S extension (pull-apart basin), (d) whole-crustal N–S extension with flat Moho, (e) upper crustal N–S extension and lower crustal channel flow in which the arrow shows the flow direction, (f) 'drop down' basin, (g) (predominantly) upper crustal N–S extension in which the dashed line shows a Moho uplift of 3 km assuming a total crustal thickness of 30 km outside the basin. *Key*: M: Moho.

The geological formations exposed along the DESIRE WRR profile range in age from Quaternary to Cretaceous (Fig. 3). In the Zohar-8 deep borehole, which lies about 1.3 km S of the profile near shotpoint 4 (Figs 1 and 3), Jurassic, Triassic and Permian sequences and the Zenifim formation of Precambrian age, underlie the exposed Cretaceous rocks (Gilboa *et al.* 1993). About 70 km further northwest a somewhat similar situation is encountered in the Helez-Deep-1A borehole (Figs 1 and 3), in which the oldest sedimentary rocks are of Permian age and the top of the Precambrian metamorphic basement occurs at 5 978 m depth. Within the DSB the El Lisan 1 borehole, which is located about 1 km S of the profile near shotpoint 6 (Figs 1 and 3), penetrated the salt-rich Sedom formation of Pliocene age to a depth of 3 996 m below sea level (Kashai & Croker 1987). On the east side of the DST rocks of Cretaceous age can be seen to overlie rocks of Cambrian age about 15 km south of shotpoint 7 and in the bottom of a deep wadi just a few kilometres south of the profile east of shotpoint 7. Thus around shotpoint 7 the thickness of the section overlying the rocks of Cambrian age is only a few hundred metres. Around shotpoint 8, the profile crossed basalts of Cenozoic age for about 20 km (Figs 1 and 3). East of the DST, the closest borehole to the WRR profile in which rocks of Precambrian age are encountered is the Al Jafr borehole about 110 km south of the profile (Fig. 1). In this borehole rocks of Permian age are in contact with rocks of Silurian age at about 400 m depth and rocks of the Saramuj formation of Precambrian age are encountered at 3 336 m depth and continue down to the base of the hole at 4 048 m depth. The Saramuj formation has similar lithologies and age as the Zenifim formation west of the DSB.

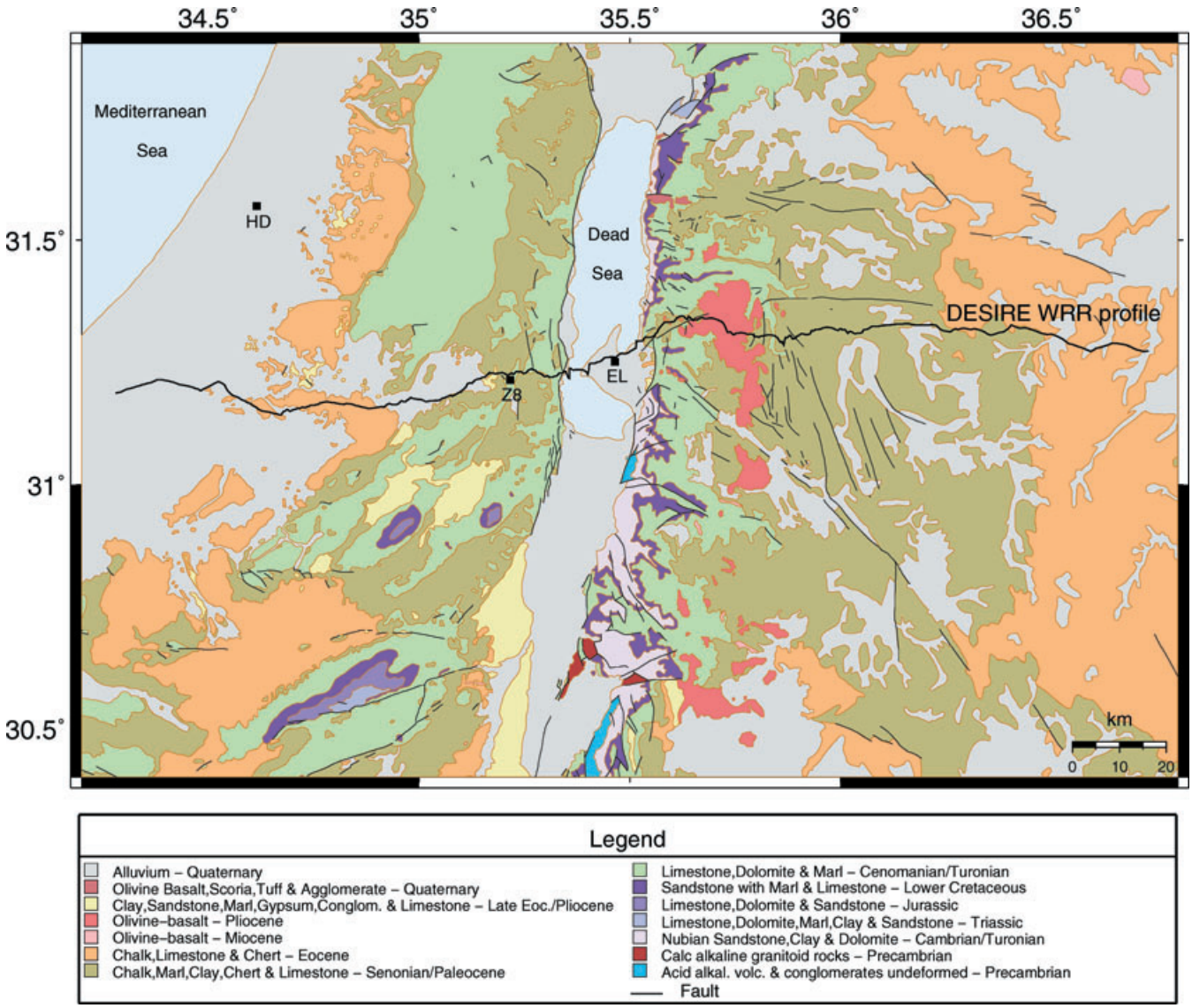

Figure 3. Geological map, simplified from Bartov (1990), of the Dead Sea region. The position of the DESIRE wide-angle reflection/refraction (WRR) profile is shown as are the positions of the Helez-Deep-1A (HD), Zohar-8 deep (Z8) and El Lisan 1 (EL) boreholes.

The DESIRE seismic WRR profile is 235 km long and trends more or less E–W from the Jordanian highlands in the E to the Israeli–Egyptian border in the W. The profile crosses the DST at the latitude of the Lisan peninsula which is more or less in the middle of the southern part of the DSB. The experiment comprised on the source side, 11 borehole shots which were recorded by 200 three-component instruments and 400 one-component instruments. Of the 11 shots, five were large shots (shot nos. 1, 3, 6, 9 and 11 in Fig. 1) with charge sizes of 1000 kg. They were executed with the aim of obtaining the whole crustal structure and, in particular, the wide-angle reflection from the crust–mantle boundary (Moho). The other six shots (nos. 2, 4, 5, 7, 8 and 10 in Fig. 1) were small shots with charge sizes of 250 kg. They were executed with the aim of obtaining the detailed structure of the top of the seismic basement, which is here defined as the top of the layer with *P*-wave velocities greater than 5.6 km s^{-1}. The 11 shots were recorded by 200 three-component seismometers mainly spaced 1.2 km apart along the whole length of the profile and 400 vertical seismometers interspersed between the three-component instruments. This resulted in a 300 m instrument spacing along the central 150 km of the profile, a 600 m spacing along the next 18 km of the profile on both sides and finally a 1.2 km spacing for the outer 20–25 km at both ends. Across the western part of the DSB, the instruments were sited on the lower levels of large dams, which have been constructed in connection with the extraction of potash from the Dead Sea. Thus the instrument spacing of 300 m could be maintained across the whole width of the DSB (Figs 1 and 3).

Previous crustal-scale WRR experiments in the study area include that in Israel in 1977 (Ginzburg *et al.* 1979a, b), the onshore-offshore experiment between southern Israel and Cyprus in 1978 (Makris *et al.* 1983; Ben-Avraham *et al.* 2002) and that in Jordan in 1984 (El-Isa *et al.* 1987a,b). In addition, an onshore-offshore experiment was carried out along the Dead Sea, just west of the axis of the Dead Sea basin (DSB, Ginzburg & Ben-Avraham 1997). The majority of the profiles completed in these experiments trended more or less N–S and none of them actually crossed the DST or the DSB. The first WRR experiment to cross the DST was the DEad SEa Rift

Transect (DESERT) in 2000 (Weber *et al.* 2004; Mechie *et al.* 2005). The DESERT profile crosses the DESIRE profile at the common shotpoint no. 1 (Fig. 1). Finally, in autumn 2004 the U.S. Geological Survey (USGS) completed two WRR profiles in the study area. One of these was a N–S profile along the DST structure. The other was a NW–SE profile more or less parallel to the DESERT profile (Fig. 1). This profile crossed the DST about 30 km S of the DESIRE profile, about 50 km N of the DESERT profile and just N of the Amazyahu Fault which marks the southern limit of the southern DSB (ten Brink *et al.* 2006). It crossed the DESIRE profile 5 km E of DESIRE shot no. 3. Comparisons between the results obtained from these previous seismic experiments and those obtained from the DESIRE experiment will be made below in the discussion and summary section.

DATA AND PHASE CORRELATIONS

Figs 4–9 show data examples from eight shots. These shot gathers show the compressional (*P*) seismic wavefield resulting from the vertical component of ground motion. They are displayed in the form of distance versus reduced-time record sections in which, for clarity, no more than 60 km distance range is shown in any one figure. Shot gathers for the shear (*S*) seismic wavefield resulting from the horizontal components of ground motion, show that *S*-waves were not well recorded.

Seven seismic phases have been recognized in the record sections. For six of these phases arrival times have been picked and used in the *P*-wave modelling (Tables 1–3). During the picking, each individual arrival was assigned a quality of 1, 2 or 3. Clear, sharp onsets, which are mainly first arrivals at shorter distances (see e.g. Fig. 6b) were assigned a travel-time error of ± 0.05 s. Less clear onsets, which are mainly first arrivals at larger distances and the clearer reflections (see e.g. phase *PmP* between 100 and 110 km distance range in Fig. 4a) were assigned a travel-time error of ± 0.1 s. The least clear onsets which are mainly the less clear reflections (see e.g. phase *PmP* beyond 110 km distance in Fig. 4a) were assigned a travel-time error of ± 0.2 s. The root mean square of the travel-time errors is provided for each phase in Table 3, from which it can be seen that the root mean square error for phase *Pg* is close to 0.1 s or pick quality 2. The root mean square errors for the other phases are close

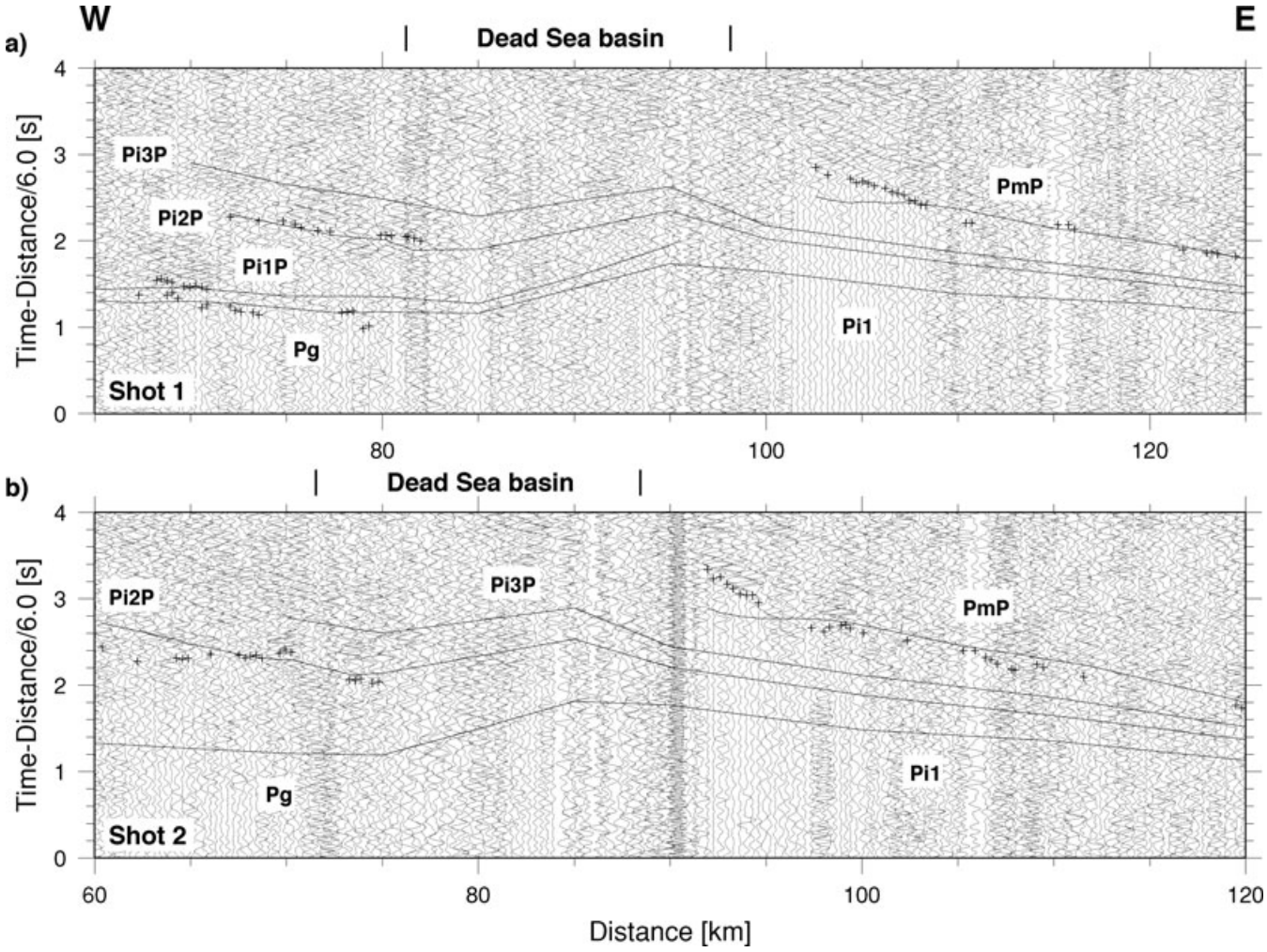

Figure 4. Seismic data from (a) shot 1 and (b) shot 2 recorded along the WRR profile. The record sections show the vertical component of *P*-wave motion for the distance ranges 65–125 km east of the shotpoint in the case of shot 1 and 60–120 km east of the shotpoint in the case of shot 2, reduced with a velocity of 6 km s^{-1}. Each trace is normalized individually and bandpass filtered from 4 to 12 Hz. Lines represent phases calculated from the model in Fig. 11a, while crosses represent observed travel times. The position of the DSB is marked. *Key*: *Pg*: first arrival through the upper crust above 11 km depth, *Pi1P*: reflection from the top of the layer at about 11 km depth outside the DSB, *Pi1*: first arrival through the upper crust below 11 km depth, *Pi2P*: reflection from the top of the lower crust, *Pi3P*: reflection from the top of the lower layer in the lower crust, *PmP*: Moho reflection.

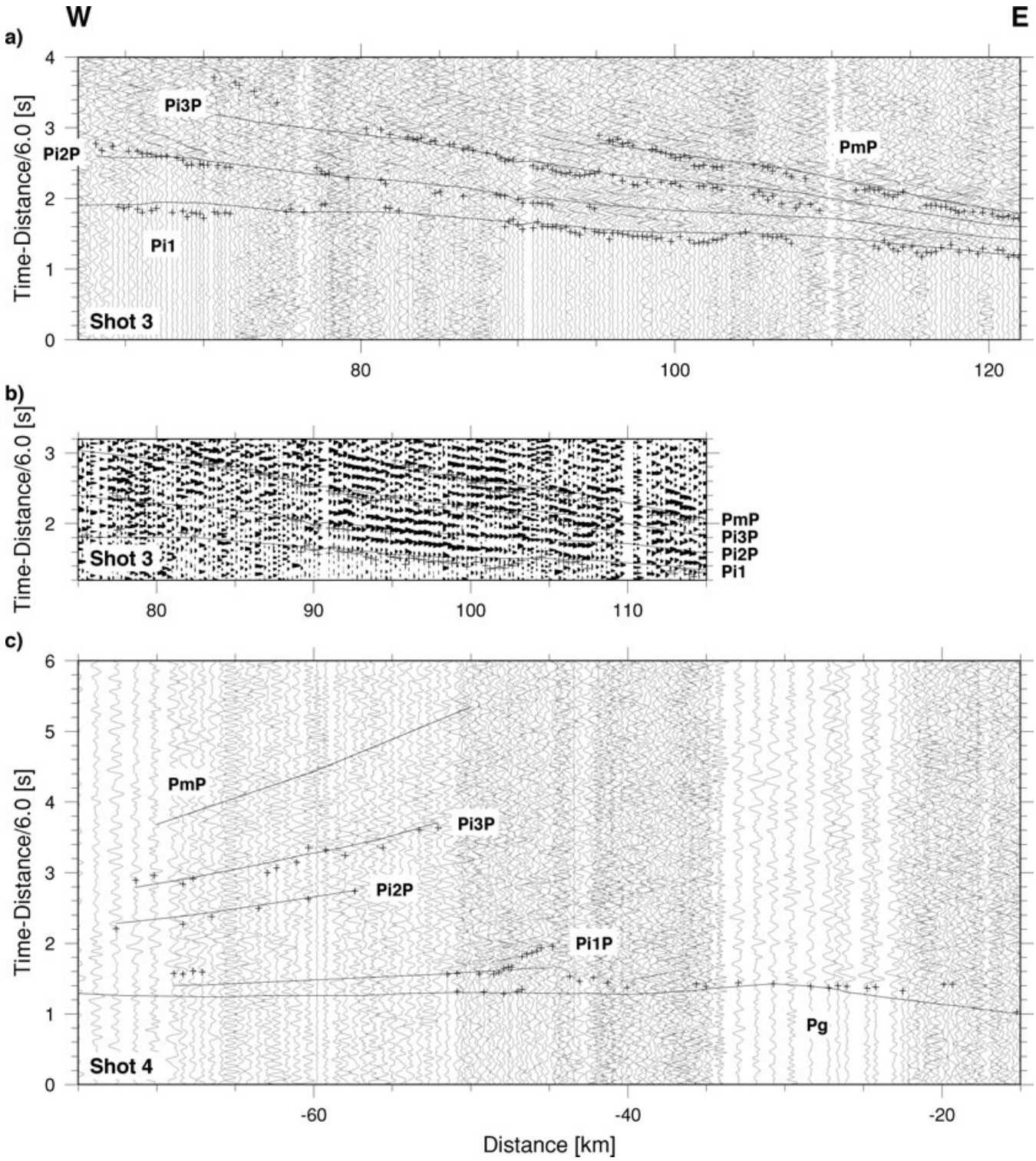

Figure 5. Seismic data from (a) and (b) shot 3 and (c) shot 4 recorded along the WRR profile. The record sections show the vertical component of *P*-wave motion for the distance ranges (a) 62–122 km and (b) 75–115 km east of the shotpoint, east of the Dead Sea basin in the case of shot 3 and (c) 15–75 km west of the shotpoint, west of the Dead Sea basin in the case of shot 4. The data are processed and presented as in Fig. 4, except for (b) in which only negative filled amplitudes are shown, in order to highlight the coherence of the phases, especially *Pi3P*. *Key*: see Fig. 4.

to 0.2 s, which is due to the fact that the majority of the picks for these phases have a quality of 3.

The first phase, the first arrival, *Pg*, is observed in the record sections from all shots (Table 1). Over the first few tens of kilometres distance in the record sections, the phase can be split into two or three distinct branches each with an apparent velocity significantly less than 6 km s^{-1}. Beneath shots 1–4 in the western part of the profile, the first branch out to a distance of about 2 km has apparent velocities between 2.2 and 3.0 km s^{-1}. The next branch beneath shots 1–4, is also the first branch beneath shots 5–11. It can be observed out to

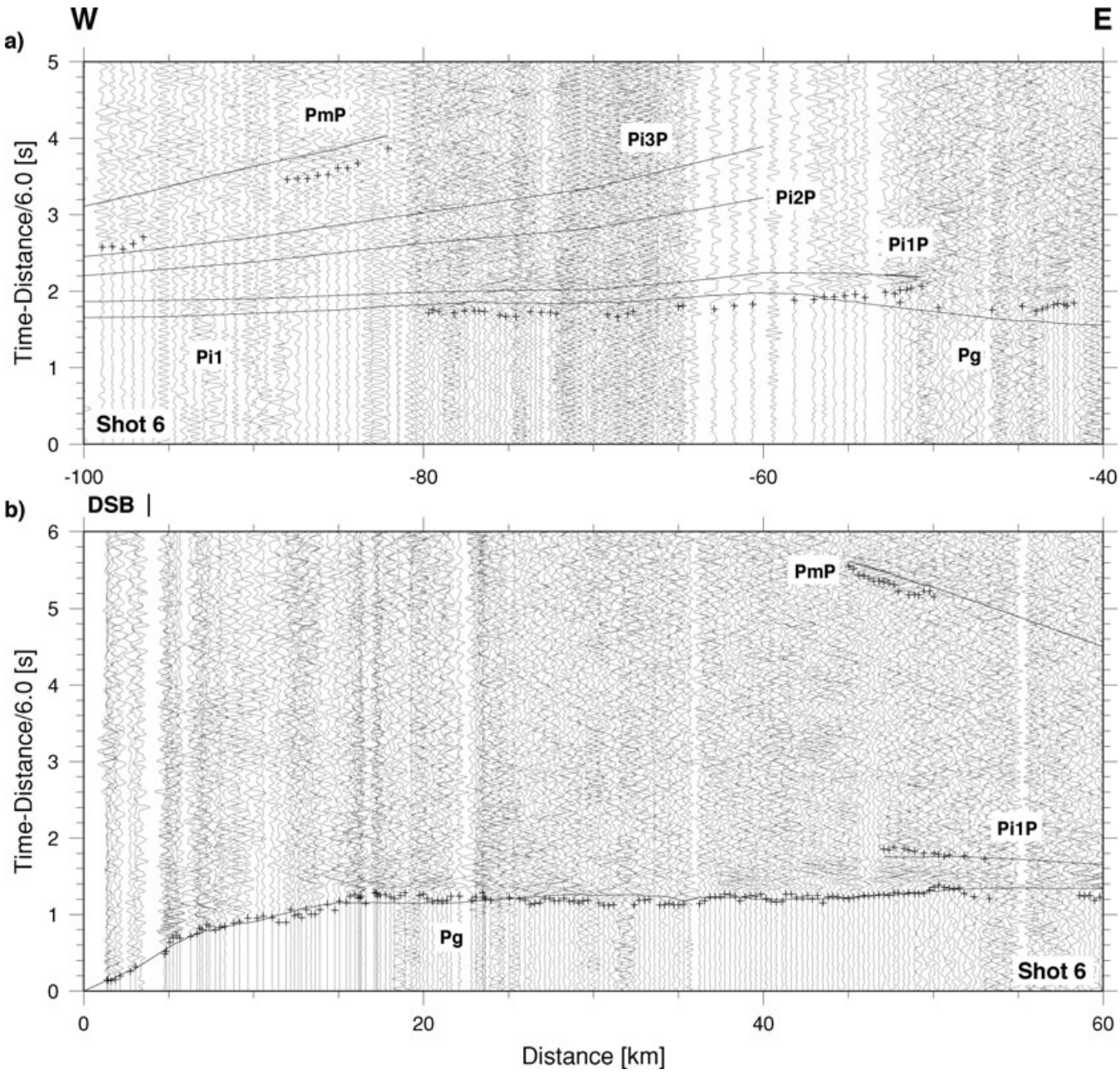

Figure 6. Seismic data from shot 6 recorded along the WRR profile. The record sections show the vertical component of *P*-wave motion for the distance ranges (a) 40–100 km west of the shotpoint, west of the DSB and (b) 0–60 km east of the shotpoint. The position of the eastern boundary of the DSB is marked. The data are processed and presented as in Fig. 4, except that the data from shot 6 are bandpass filtered from 4 to 15 Hz. *Key*: see Fig. 4.

a maximum distance of about 13 km and has apparent velocities from 2.6 to 4.4 km s^{-1}. The next branch can be observed out to a maximum distance of about 34 km in the western portion of the profile and has apparent velocities from 3.7 to 5.4 km s^{-1}. The main branch of *Pg* has average apparent velocities from 5.65 to 6.2 km s^{-1} and can be observed out to maximum distances of around 95 km. Significant travel-time delays of this phase up to about 0.7 s generally occur as it enters the DSB as exemplified in the record section from shotpoint 9 (Fig. 8b). At larger distances, *Pi1*, from the basal layer of the upper crust, succeeds *Pg* as the first arrival. It can be recognized on the record sections from shotpoints 3 and 9 (Figs 5a and 8a–b) out to maximum distances of about 140 km. The average apparent velocities for this phase are 6.4–6.5 km s^{-1} which are a little higher than those for *Pg*.

In addition to the two first arrival phases, four reflected phases have been identified (Table 1). The presented shot gathers show all the picked arrivals for three of these reflected phases, *Pi1P*, *Pi2P* and *Pi3P* and 80% of the picked arrivals for the fourth reflected phase, *PmP*. Sometimes clear onsets are visible for these phases, for example phase *PmP* from shot 1 between 100 and 110 km distance (Fig. 4a) and *PmP* from shot 2 between 90 and 100 km distance (Fig. 4b). Often, however, the reflected phases are characterized by an increase in energy and individual onsets are rather difficult to identify, although phase correlation from trace to trace is often

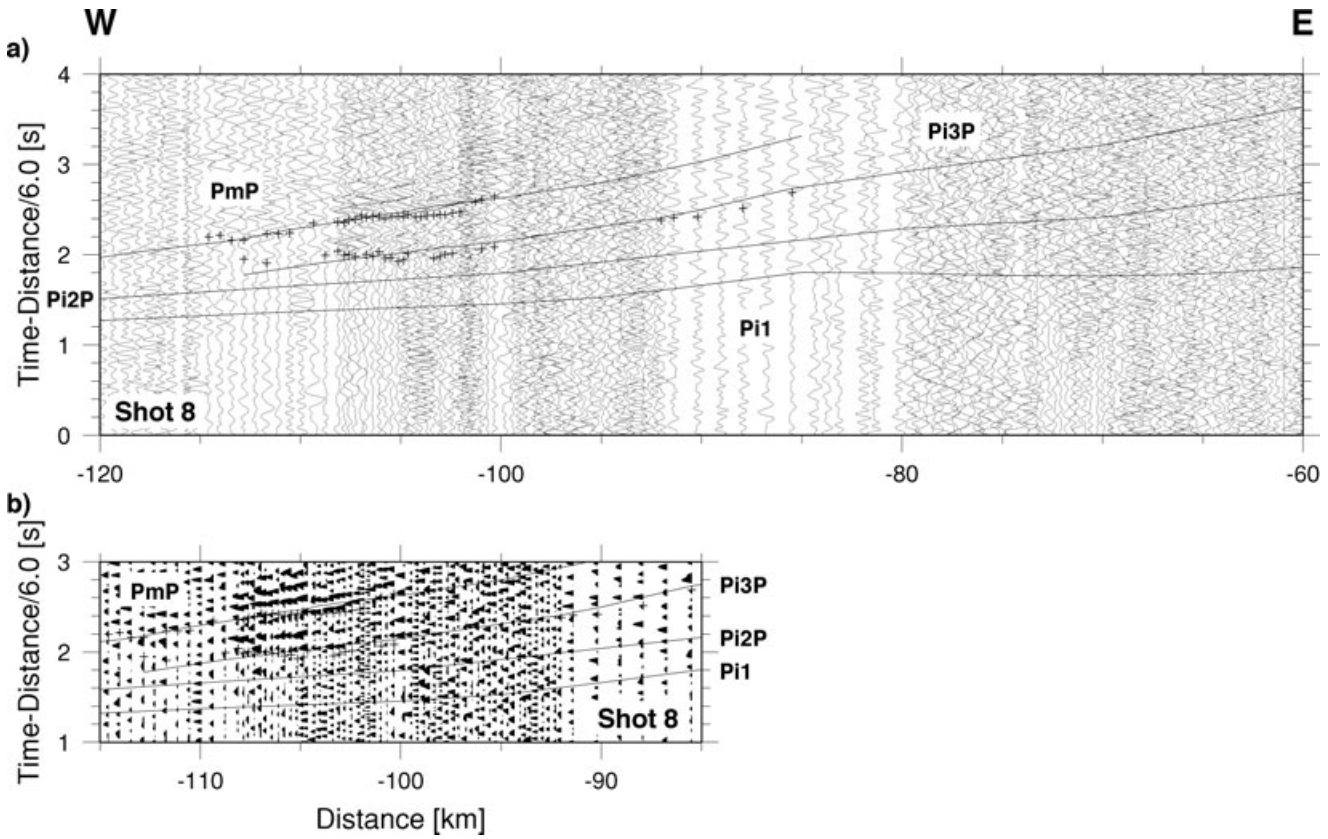

Figure 7. Seismic data from shot 8 recorded along the WRR profile. The record sections show the vertical component of *P*-wave motion for the distance ranges (a) 60–120 km and (b) 85–115 km west of the shotpoint, west of the Dead Sea basin. The data are processed and presented as in Fig. 4, except for (b) in which only positive filled amplitudes are shown, in order to highlight the coherence of the phases, especially *Pi3P*. *Key*: see Fig. 4.

good over distances of several kilometres, for example *PmP* from shot 8 between 100 and 110 km distance (Fig. 7). The first of these phases, *Pi1P*, is the reflection from the top of the basal layer of the upper crust and is thus the reflected phase associated with the first arrival refracted phase, *Pi1*. *Pi1P* can be recognized on the record sections from shots 1, 4 and 6 (Figs 4a, 5c and 6a-b) up to about 1 s behind *Pg* between about 40 and 70 km distance range. The second reflected phase, *Pi2P*, is the reflection from the boundary between the upper and lower crust. It can be recognized on the record sections from shots 1, 2, 3, 4, 9 and 11 (Figs 4–5 and 8–9) between 60 and 115 km distance range and 1.6–2.8 s reduced time. The third reflected phase, *Pi3P*, is a reflection from a boundary within the lower crust. It can be seen on the record sections from shots 3, 4, 6, 8 and 9 (Figs 5–8) between 50 and 130 km distance range and 1.4–3.8 s reduced time. On the record section from shot 3 it can be correlated over a distance of 35–40 km (Figs 5a and b), on that for shot 8 over a distance of 25–30 km (Fig. 7) and on that for shot 4 over a distance of 20 km (Fig. 5c). For this phase, 22 arrival times were picked from four shots along the DESERT profile, although the boundary associated with this phase was not included in the final model for the DESERT profile (Weber *et al*. 2004). In contrast, 128 arrival times for this phase were picked from the DESIRE profile. This is in fact more than were picked for phase *Pi2P* (Table 1). Thus it is thought to be justified to include the boundary associated with this phase in the final model for the DESIRE profile. The last reflected phase, *PmP*, is the reflection from the crust–mantle boundary (Moho). This phase can be recognized on the record sections from shots 1, 2, 3, 6, 8, 9 and 11 (Figs 4–9) between 45 and 150 km distance range and 1.0–5.8 s reduced time. On the record sections from shots 1, 2, 3 and 9 this phase can be correlated over distance ranges of 30–50 km. On the record section from shot 3, it is possible that one picked arrival at about 150 km distance range and 0.7 s reduced time belongs to the *Pn* phase, the first arrival refracted phase through the uppermost mantle. Finally, on the record section from shot 11, there is a prominent late phase, marked 'X' (Fig. 9). This phase actually shows decreasing travel times with increasing distance and thus has a negative average apparent velocity out to about 83 km distance, beyond which travel times increase again. Whether this phase is associated with the shot or originates from another source is a subject of ongoing research.

MODELLING AND RESULTS

Based on the phase correlations and picking described above, 1-D velocity-depth models were constructed for each shot in each of the two directions using both travel times and amplitudes. These 1-D velocity-depth models were calculated using trial-and-error forward modelling in which theoretical travel times were calculated using ray-tracing methods (see, for example, Červený *et al.* 1977) and theoretical seismograms were calculated using the reflectivity method (Fuchs & Müller 1971).

Two-dimensional modelling was carried out mainly by inversion of the travel times supplemented by forward modelling of the amplitudes. Generally, the 1-D models were combined to provide 2-D layered, initial models of varying complexity. These initial models were developed into end models using inversion for both layer boundaries and *P*-wave velocities. However, as an alternative for the

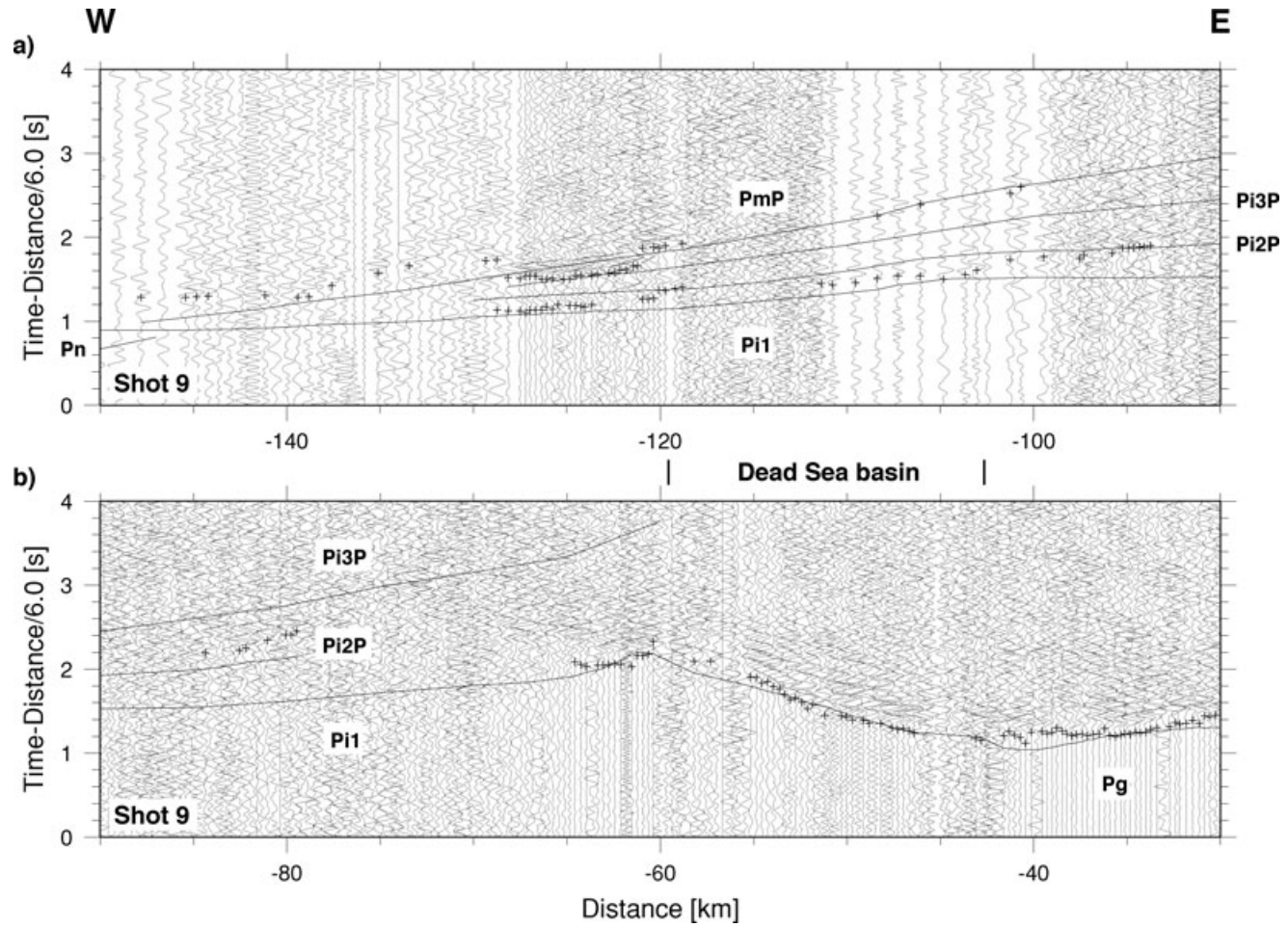

Figure 8. Seismic data from shot 9 recorded along the WRR profile. The record sections show the vertical component of *P*-wave motion for the distance ranges (a) 90–150 km west of the shotpoint, west of the DSB and (b) 30–90 km west of the shotpoint. The position of the DSB is marked. The data are processed and presented as in Fig. 4. *Key:* see Fig. 4.

upper crust, a tomogram of the *P*-wave velocity field was derived using all the arrivals of the *Pg* and *Pi1* phases. For the modelling of the travel times, the forward problem was solved by finite-differences ray-tracing based on the eikonal equation (Vidale 1988; Podvin & Lecomte 1991; Schneider *et al.* 1992). A grid size of 50 × 50 m was used. Partial derivatives of the calculated travel times with respect to the velocity and/or interface nodes were then derived using the techniques described by Lutter & Nowack (1990), Lutter *et al.* (1990) and Zelt & Smith (1992). Subsequently, a damped least-squares inversion with or without added flattening or smoothing of the model (see, for example Zelt & Smith 1992; Zelt & Barton 1998) was carried out to obtain updates for the velocity and/or interface nodes, and the forward and inverse problems were repeated until an acceptable convergence between the observed and calculated travel times was obtained. To supplement and guide the travel-time modelling, amplitudes were calculated using a finite-difference approximation of the wave equation for 2-D heterogeneous elastic media by Kelly *et al.* (1976) with transparent boundary conditions (Reynolds 1978) and implemented by Sandmeier (1990).

The travel-time modelling was carried out using a top-to-bottom approach. For the model with several discrete layers in the upper crust the modelling was done in five steps, namely upper upper crust (*Pg* phase), boundary within upper crust and lower upper crust (*Pi1P* and *Pi1* phases), boundary between upper and lower crust (*Pi2P* phase), upper lower crust and boundary within lower crust (*Pi3P* phase) and lower lower lower crust and Moho (*PmP* phase). This model will be referred to as model 1, hereafter. In total, 2811 travel-time readings were used in the inversion to derive this model (Table 1), which contains 38 independent velocity and interface depth parameters (Tables 2 and 3). Velocities were defined at the top and bottom of each layer usually at 5–20 km intervals along the profile. During the inversion the velocities at the top and bottom of each layer for any particular node were always constrained to be updated by the same amount. Although the velocities and interface depths in the model were usually specified at 5–20 km intervals along the profile, in the inversion a smaller number of independent velocity and interface depth parameters was solved for by grouping individual nodes together and constraining them to move by the same amount (Table 2). As a consequence of the inversion, the resolution and standard errors for the various parameters can be calculated (Table 2). These standard error estimates should be viewed as lower bounds of the true errors (Zelt & Smith 1992) and more realistic values are also provided (Table 2). Although lower crustal velocities were not inverted for in the travel-time inversions, from forward modelling of the relative amplitudes of the reflected phases *Pi2P*, *Pi3P* and *PmP* and from previously determined lower crustal velocities in the area (e.g. Ginzburg *et al.* 1979a; El-Isa *et al.* 1987a; Weber *et al.* 2004), it is estimated that realistic error bounds for the velocities for the two lower crustal layers are ± 0.2 km s^{-1}.

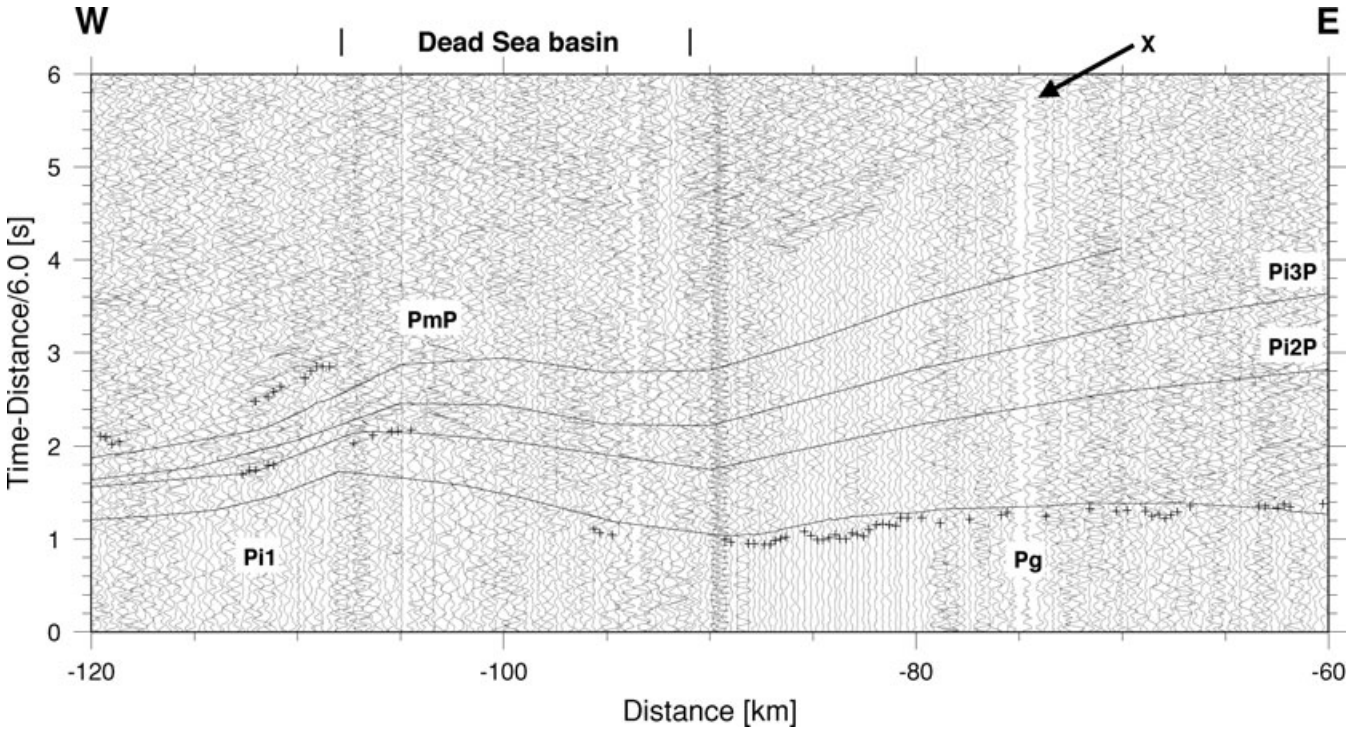

Figure 9. Seismic data from shot 11 recorded along the WRR profile. The record section shows the vertical component of *P*-wave motion for the distance range 60–120 km west of the shotpoint. The position of the Dead Sea basin is marked. The data are processed and presented as in Fig. 4. *Key*: see Fig. 4 and X—prominent late phase.

Table 1. Number of travel times picked for each phase from each shot and used in the inversion for models 1 and/or 2.

Shot	1	2	3	4	5	6	7	8	9	10	11	Total
Phase												
Model 1												
Pg	118	111	230	131	78	369	253	214	266	159	172	2 101
	17	18	24	20	9	34	24	22	24	18	23	
Pi1P	9			18		19						46
	2			4		4						
Pi1			133						40			173
			17						8			
Model 2												
Pg/Pi1	118	111	363	131	78	377	258	214	308	159	175	2 292
Models 1 and 2												
Pi2P	14	19	43	6					18		10	110
	3	4	8	4					5		4	
Pi3P			64	13		5		26	20			128
			9	6		2		7	3			
PmP	40	30	91			36		32	21		13	253
	8	6	11			14		2	8		3	

Note: In the second row, the number of rays plotted in Fig. 12 is given.

For the model with the tomogram of the upper crust, the modelling was done in four steps, namely upper crust (*Pg* and *Pi1* phases), boundary between upper and lower crust (*Pi2P* phase), upper lower crust and boundary within lower crust (*Pi3P* phase) and lower lower crust and Moho (*PmP* phase). This model will be referred to as model 2, hereafter. For the derivation of this model 2783 travel-time readings were utilized (Table 1). The upper crustal tomogram is defined by 539 velocity nodes with a node spacing of 5 km in the horizontal direction and 2 km in the vertical direction. As the LSQR method (Paige & Saunders 1982; Nolet 1987) was used for the inversion, no formal resolution or standard error estimates are available. As a proxy for the resolution the number of rays, which passed within two node spacings of any one particular node was utilized. It is thought that realistic error values for the upper crustal velocities in this model are ± 0.1 km s^{-1} or better in areas of good ray coverage and up to ± 0.2 km s^{-1} in areas of poor ray coverage. The remainder of this model has eight independent interface depth nodes (Table 2), which is the same number as model 1. Realistic errors for the interface depths and layer velocities in the lower crust in this model are thought to be similar to those for model 1.

Upper crustal structure for model 1

The upper crustal structure for model 1 was derived in two steps. In the first step, 2101 *Pg* phase arrivals were utilized to derive the structure of the upper upper crust, also termed the seismic basement. This involved the determination of the layer velocities and interface depths down to just above the interface at about 11 km depth. Initial models of various complexities were derived partly based on the 1-D models and partly based on previous geophysical and geological studies of the DSB. The initial model (Fig. 10a) for the inversion which led to the preferred final model (Fig. 11a) was based on the 1-D models outside the DSB. The DSB structure itself was mainly a simplified version of a gravity model across the basin about 20 km south of the seismic profile (Ben-Avraham & Schubert 2006) and the seismic model from profile DSP (Fig. 1) along the basin (Ginzburg & Ben-Avraham 1997). The positions of the steeply-dipping master faults on the east and west sides of the basin were also based on local geological

Table 2. Some input parameters for the inversions and the resolution (R) and calculated standard errors after Zelt & Smith (1992) for the various nodes for the final iteration and realistic standard errors for the various layer velocities and interface depths.

Parameter type	No. of nodes	R	Calc. std. error (km s^{-1} or km)	Realistic std. error (km s^{-1} or km)	Node coordinates (km)
First layer velocity	2	0.998	0.02	0.2	106, 108
		0.998	0.02		121, 123.1
Second layer velocity	1	0.976	0.08	0.2	0, 15, 25, 35, 45, 55, 65, 75, 85, 90, 95
Third layer velocity	4	0.996	0.03	0.2	0, 15, 25, 35, 45, 55
		0.994	0.04		65, 75, 85, 90, 95, 100, 105
		0.999	0.02		125, 130, 135, 145, 155, 165, 175
		0.997	0.03		185, 195, 205, 215, 225, 240
Fourth layer velocity	4	0.999	0.02	0.2	0, 15, 25, 35, 45, 55
		0.998	0.02		65, 75, 85, 90, 95, 100, 105
		0.997	0.03		125, 130, 135, 145, 155, 165, 175
		0.995	0.03		185, 195, 205, 215, 225, 240
Fifth layer (seismic basement) velocity	4	0.996	0.03	0.1	0, 15, 25, 35, 45, 55
		0.999	0.02		65, 75, 85, 90, 95, 100, 105
		0.9998	0.01		125, 130, 135, 145, 155, 165, 175
		0.999	0.02		185, 195, 205, 215, 225, 240
Sixth layer (Pi1) velocity	1	0.9997	0.01	0.2	0, 15, 25, 35, 45, 55, 65, 75, 85, 90, 95, 100, 105, 110, 115, 120, 125, 130, 135, 145, 155, 165, 175, 185, 195, 205, 215, 225, 240
First interface	1	0.982	0.03	0.2	0, 10, 20, 30, 40, 50, 60, 70, 80, 90
Second interface	6	0.9997	0.05	0.5	0, 10, 20, 30
		0.9998	0.05		35, 40, 50, 60
		0.9999	0.03		70, 80, 90, 100
		0.9998	0.05		130, 140, 150, 160
		0.9999	0.03		170, 180, 190, 200
		0.9997	0.05		210, 220, 230, 240
Third interface	6	0.995	0.36	1.0	0, 10, 20, 25, 30
		0.9992	0.14		40, 50, 60, 70
		0.9998	0.07		80, 90, 100
		0.99997	0.03		130, 140, 145, 150, 160
		0.9999	0.05		170, 180, 190, 200
		0.9992	0.14		210, 220, 230, 240
Pi1P interface	1	0.08	0.06	1.0	0, 20, 40, 60, 80, 100, 109.4, 110.6, 118.4, 119.7, 140, 160, 180, 200, 220, 240
Pi2P interface (model 1)	3	0.999	0.17	2.0	0, 24, 44, 64, 84
		0.999	0.17		104, 124
		0.976	0.78		144, 164, 184, 204, 224, 240
Pi2P interface (model 2)	3	0.999	0.18	2.0	0, 24, 44, 64, 84
		0.999	0.19		104, 124
		0.973	0.82		144, 164, 184, 204, 224, 240
Pi3P interface (model 1)	2	0.997	0.29	3.0	0, 24, 44, 64, 84
		0.999	0.16		104, 124, 144, 164, 184, 204, 224, 240
Pi3P interface (model 2)	2	0.997	0.28	3.0	0, 24, 44, 64, 84
		0.999	0.16		104, 124, 144, 164, 184, 204, 224, 240
PmP interface (model 1)	3	0.996	0.31	3.0	0, 24, 44, 64, 84
		0.9993	0.13		104, 124
		0.998	0.23		144, 164, 184, 204, 224, 240
PmP interface (model 2)	3	0.997	0.29	3.0	0, 24, 44, 64, 84
		0.9992	0.14		104, 124
		0.998	0.23		144, 164, 184, 204, 224, 240
PmP* interface (model 1)	3	0.996	0.31	3.0	0, 24, 44, 64, 84
		0.9996	0.10		104, 124
		0.998	0.24		144, 164, 184, 204, 224, 240
PmP* interface (model 2)	3	0.997	0.28	3.0	0, 24, 44, 64, 84
		0.9995	0.11		104, 124
		0.998	0.24		144, 164, 184, 204, 224, 240

Note: The first layer is the top layer in the basin and the second layer is the top layer W of profile km 94. PmP* denotes the inversions without Pi3P being included in the modelling.

Table 3. Some input parameters and results of the inversions.

Phase		Pg	Pi1P + Pi1	Pi2P	Pi3P	PmP	PmP*
Parameter							
Ave. δt initial	Model 1	0.13, 3.66	0.12, 0.76	0.19, 1.72	0.13, 0.48	0.20, 2.15	0.24, 2.85
model (s), χ^2	Model 2	0.36, 19.38		0.12, 0.56	0.16, 0.68	0.15, 1.05	0.31, 4.31
Ave. δt final	Model 1	0.11, 1.85	0.10, 0.47	0.11, 0.37	0.12, 0.43	0.15, 0.95	0.13, 1.03
model (s), χ^2	Model 2	0.06, 0.48		0.10, 0.29	0.12, 0.47	0.12, 0.58	0.15, 1.01
σ_d (s)	Model 1	0.11	0.17	0.18	0.19	0.18	0.18
	Model 2	0.12		0.18	0.19	0.18	0.18
σ_m-interface (km)		0.2, 3.0, 5.0	0.06	5.0	5.0	5.0	5.0
σ_m-velocity (km s^{-1})		0.5	0.5				
D		1.0	1.0	1.0	1.0	1.0	1.0

Note: σ_d is the root mean square of the standard deviations of the travel-time readings, σ_m is the *a priori* uncertainty in the model parameters and D is the overall damping factor (see, for example, Zelt & Smith 1992). PmP* denotes the inversions without Pi3P being included in the modelling.

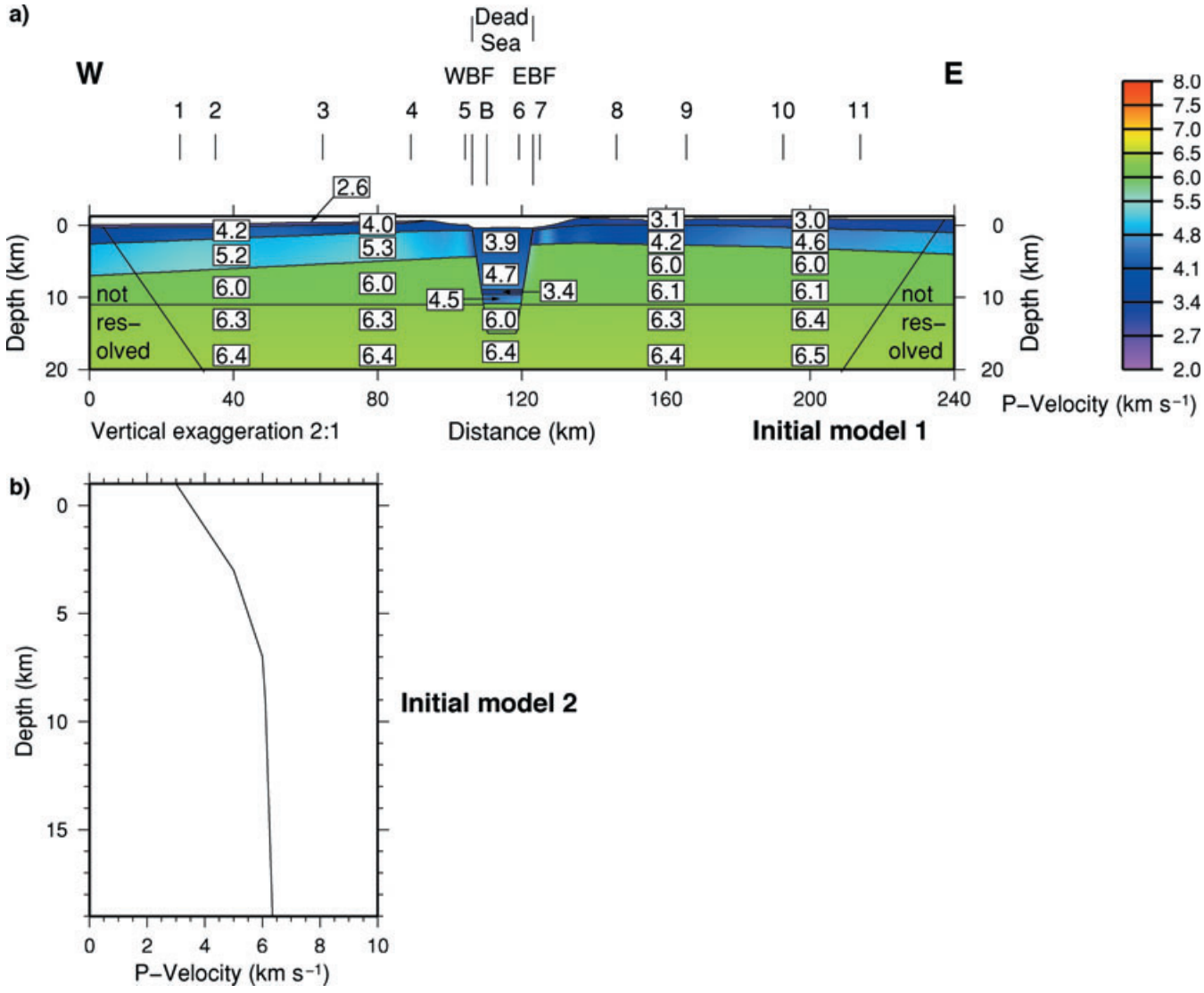

Figure 10. (a) Two-dimensional initial *P*-wave velocity model (velocities in km s^{-1}) for the inversion, which produced the model shown in Fig. 11(a). (b) 1-D initial *P*-wave velocity model for the tomography that produced the upper crustal part of the model shown in Fig. 11b. The positions of the shotpoints are marked above the 2-D model. *Key*: WBF: Western Boundary Fault, EBF: Eastern Boundary Fault, B: international boundary.

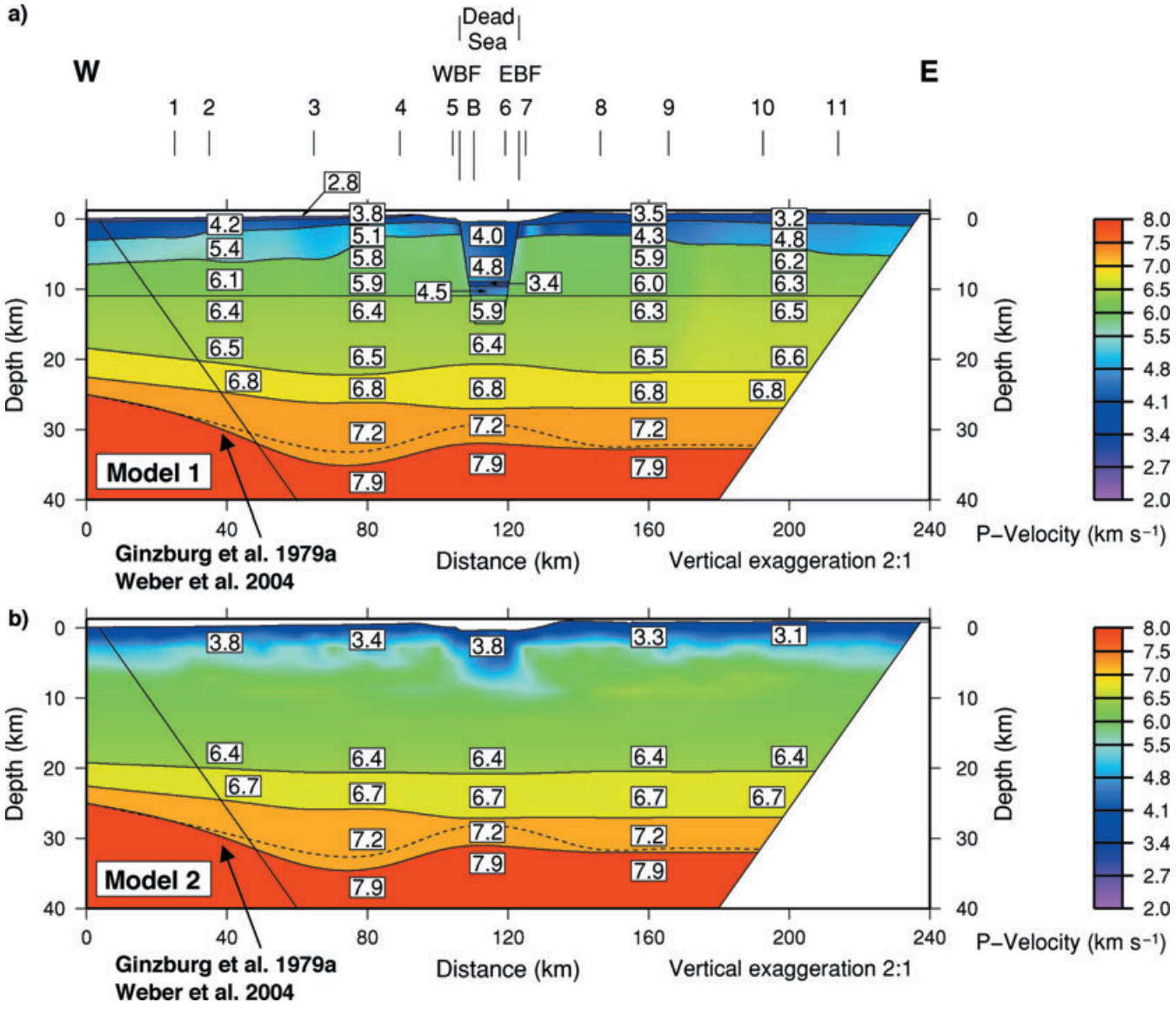

Figure 11. Two-dimensional *P*-wave velocity models for the DESIRE wide-angle reflection/refraction (WRR) profile. (a) Model with several discrete layers in the upper crust. (b) Model with tomogram of the upper crust. Only the area inside the diagonal lines is resolved in this study. Outside this area to the west the model is based on previous studies, for example Ginzburg *et al.* (1979a) and Weber *et al.* (2004). Velocities in km s^{-1}. The positions of the shotpoints are marked above the 2-D models. *Key*: see Fig. 10.

observations of where the seismic line actually crossed the basin edges. The positions of these faults, the thicknesses of the top three layers within the basin and the velocities of the second and third top layers within the basin were kept fixed during the inversion. The initial model outside the basin had laterally varying velocities in the top three layers west of the basin and in the top two layers east of the basin. In addition each of the interfaces east and west of the basin had approximately uniform dips away from the basin (Fig. 10a). The seismic basement had a uniform velocity of 6.0 km s^{-1} along its top surface and 6.1 km s^{-1} along its bottom surface. Four iterations, after which no further significant improvement seemed to be occurring, were required in order to reach the final model. In the first iteration five independent interface nodes and seven independent velocity nodes were solved for, while in the last two iterations 13 independent interface nodes with *a priori* uncertainty estimates from 0.2 to 5.0 km and 15 independent velocity nodes with *a priori* uncertainty estimates of 0.5 km s^{-1} were solved for (Tables 2 and 3). The root mean square travel-time residual reduced from 0.13 s ($\chi^2 = 3.66$) to 0.11 s ($\chi^2 = 1.85$) during the inversion (Table 3). This reduction is significant according to the *F* test at the 95% confidence limit. The χ^2 value of 1.85 and the fact that the root mean square travel-time residual for the final model is close to the average standard deviation of the picked travel-time data (Table 3) indicate that the data are adequately but not over fitted. Inspection of the resolution matrix shows that all of the model parameters are well resolved and that all off-diagonal elements of the resolution matrix are small compared to the diagonal elements. However, as the ray diagram shows (Fig. 12a), not all regions of the model are equally resolved. In particular, the deeper parts of the seismic basement, including the DSB, below about 7 km are not well resolved.

Outside the DSB, the top layer in the western part of the model has a low average velocity of about 2.8 km s^{-1} and a thickness of just a few hundred metres (Fig. 11a). The next layer, which is

also the top layer east of the DSB, has average velocities of 3.2–4.2 km s^{-1} and thicknesses of up to about 3 km. In general, the base of this layer dips downwards away from the DSB, although this is much more apparent west of the basin than east of it. The next layer has velocities of 4.3–5.4 km s^{-1} and thicknesses of up to about 4 km. Again the base of this layer generally dips downwards away from the DSB, although west of the basin the greatest thickness of this layer occurs between profile km 40 and 70. The seismic basement has velocities of 5.8–6.3 km s^{-1}. The lowest velocities of 5.8–6.0 km s^{-1} occur in the vicinity of the DSB. Away from the basin, toward the west and especially toward the east, the velocities of the seismic basement increase to 6.1–6.3 km s^{-1}. Depths to the top of the seismic basement range from about 2 km below topography adjacent to the basin on both its east and west sides to about 6 km below topography at the eastern end of the profile and 6–7 km below topography almost everywhere west of profile km 70. Within the DSB the average velocity at the surface is about 4.0 km s^{-1}, increasing to about 4.8 km s^{-1} at about 8.5 km depth. There is also a tendency for higher velocities under the western portion of the basin with respect to the eastern portion. The top layer which is taken to be equivalent to the Cenozoic basin fill is 8.5 km thick and the depth to the seismic basement is 10.5 km below topography. The second and third top layers within the basin correspond to the top two layers adjacent to the master faults on both sides of the basin. The exposed geology provides evidence that the top two layers adjacent to the master faults outside the basin were deposited before the basin started to form and it is a reasonable assumption that these two layers were continuous across the area now occupied by the basin, before the basin started to form. In the final model, the thicknesses of the second and third top layers within the basin are smaller than the thicknesses of the top two layers adjacent to the master faults outside the basin. This is a reasonable situation as these two layers have certainly been involved in any extension which occurred during the basin formation.

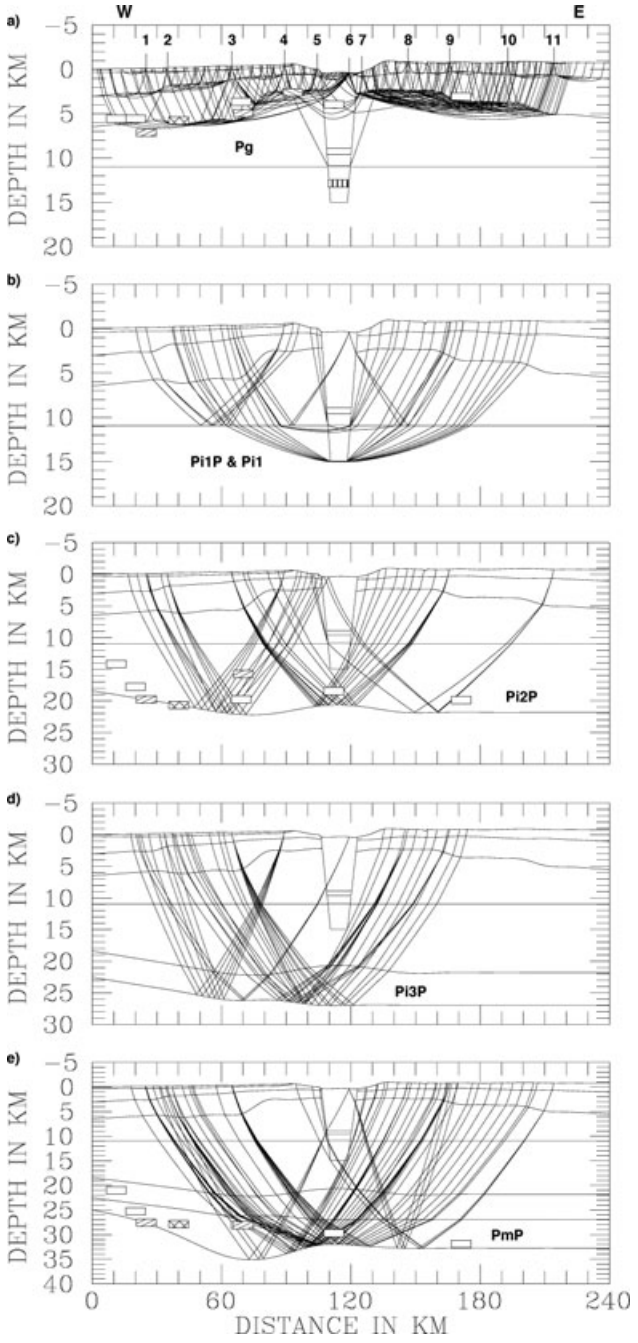

Figure 12. Summary ray diagrams for the final iterations of the (a) *Pg* phase, (b) *Pi1P* and *Pi1* phases, (c) *Pi2P* phase, (d) *Pi3P* phase and (e) *PmP* phase for the model shown in Fig. 11a. The elongated boxes represent the depth values for the respective interfaces (top of seismic basement, top of lower crust and Moho) from previous experiments in the area (empty boxes—Ginzburg *et al.* 1979a, El-Isa *et al.* 1987a; boxes with cross-hatched pattern—Makris *et al.* 1983; box with vertical pattern—Ginzburg & Ben-Avraham 1997; boxes with left-sloping pattern—Weber *et al.* 2004, ten Brink *et al.* 2006) and the Zohar-8 deep borehole at profile km 93 (box with right-sloping pattern). The number of rays plotted for each phase is given in Table 1. The positions of the shotpoints are marked above the uppermost ray diagram.

Other initial models have also been tested. For example, models have been tested in which the positions of the master faults bounding the basin were shifted up to 1 km either to the east or west of the positions shown here and in which the velocities of the second and third top layers within the basin were increased by up to 0.5 km s^{-1} with respect to the values shown here (Fig. 11a). Following five iterations in each case, the end models showed little difference to the final model shown here (Fig. 11a). An initial model with no *a priori* basin was also tested. However, the inversion for this model did not produce a basin, due to its trying to map significant lateral velocity variations into vertical velocity variations. Of particular interest were initial models in which the thickness of the top layer and correspondingly the depth to the seismic basement within the basin was varied. Only the seven first arrivals from shot 4 which in the final model shown here (Figs 11a and 12a) propagate beneath the base of the DSB can be used to distinguish between such models. For the final model shown here the root mean square travel-time residual for these seven arrivals is 0.09 s. For the end model in which the depth to the seismic basement is 1 km greater, not all of these seven arrivals from shot 4 propagate beneath the base of the DSB and their root mean square travel-time residual is 0.12 s. For the end model in which the depth to the seismic basement is 2 km greater, all of these seven arrivals from shot 4 propagate through the top layer within the basin and their root mean square travel-time residual is 0.13 s. For the end model in which the depth to the seismic basement is 1 km smaller, all of these seven arrivals from shot 4 propagate beneath the base of the DSB and their root mean square travel-time residual is 0.14 s. For end models in which the depth to the seismic basement is 2 km or more smaller, the root mean square travel-time residual for these seven arrivals from shot 4 is greater than 0.2 s. The only way to compensate for this is to allow the velocity at the top of the seismic basement beneath the basin to

decrease to values of less than 5.6 km s^{-1}. However, this is thought to be unlikely, as no evidence for such low velocities in the seismic basement beneath the DSB has ever been found from the previous N–S profiles, W2, W3 and DSP (Fig. 1) along the basin (Ginzburg *et al.* 1979a; Ginzburg & Ben-Avraham 1997). Thus it is thought that although only these few arrivals from shot 4 can provide evidence on the depth to the seismic basement beneath the basin and hence, correspondingly, on the thickness of the Cenozoic basin fill, the final model shown here (Fig. 11a) is the best that can be derived with the available data.

In the second step of the upper crustal modelling 46 *Pi1P* phase and 173 *Pi1* phase arrivals were used to derive the depths to the interface at about 11 km depth and the velocities of the lower upper crustal layer beneath (Table 1). The initial model consisted of a horizontal interface at 11 km depth outside the DSB, down-faulted to 15 km depth beneath the basin (Fig. 10a). In the initial model, the lower upper crustal layer west of profile km 170 had a uniform velocity of 6.3 km s^{-1} along the top surface and a uniform velocity of 6.4 km s^{-1} along the bottom surface. East of profile km 170 the initial model had uniform velocities of 6.4 and 6.5 km s^{-1} along the top and bottom surfaces respectively, of the lower upper crustal layer. The lateral change in velocity at profile km 170 was necessary in order to ensure that the lower upper crustal layer did not appear as a low velocity layer at the eastern end of the profile. In the inversion only one independent interface depth parameter and one independent velocity parameter were solved for. Thus, with respect to the initial model, no additional lateral variations were introduced in the model during the inversion. The independent velocity parameter had an *a priori* uncertainty estimate of 0.5 km s^{-1}, whereas the independent interface depth parameter had an *a priori* uncertainty estimate of only 0.06 km (Tables 2 and 3). This was necessary in order to prevent the interface from rising to shallower depths than the top of the seismic basement beneath the basin and thus violating the paths of the seven rays from shot 4, which propagate beneath the base of the DSB. However, preliminary studies of this model and other similar models without employing such a small *a priori* uncertainty estimate indicated that the interface would finally remain at about 11 km depth. Only one iteration in which the root mean square travel-time residual reduced from 0.12 s ($\chi^2 = 0.76$) to 0.10 s ($\chi^2 = 0.47$) was necessary before no further significant improvement was evident (Table 3). The data seem to be more than adequately fitted as indicated by the χ^2 value of 0.47. However, it may be that the error estimates for the picked travel-time data are too conservative (Table 3). In this respect, if one divides the travel-time error of each arrival by the square root of 2 and multiplies the overall damping factor, D, by 2 (Table 3), then the inversion algorithm produces exactly the same results as those presented here, but χ^2 is increased by a factor of 2. Inspection of the resolution matrix shows that the independent velocity parameter is well resolved whereas the independent interface depth parameter is not well resolved, mainly due to the small *a priori* uncertainty estimate. The ray diagram (Fig. 12b) shows that the limited ray coverage only justifies the small number of independent model parameters used in this step of the inversion. The boundary within the upper crust occurs at 11 km depth outside the DSB and 15 km depth beneath the DSB, although the depth beneath the DSB is poorly constrained (Fig. 11a). The lower upper crust has velocities of 6.3–6.6 km s^{-1}.

Upper crustal structure for model 2

The upper crustal structure for model 2 was derived in one step. The 2 292 picked first arrivals were treated as one phase and were used to derive the upper crustal tomogram (Table 1). The initial model (Fig. 10b) for the inversion which led to the preferred final model (Fig. 11b) was a 1-D model with velocities ranging from 3.0 km s^{-1} at -1 km depth to 6.35 km s^{-1} at 19 km depth. Three iterations, after which no further significant improvement seemed to be occurring, were necessary in order to reach the final model. For the inverse problem a grid size of 5 × 2 km was used, resulting in 539 nodes. *A priori* uncertainty estimates for the velocities of 1 km s^{-1} were used. An overall damping factor of 60 was used, but no further smoothing or flattening. The root mean square travel-time residual reduced from 0.36 s ($\chi^2 = 19.38$) to 0.06 s ($\chi^2 = 0.48$) (Table 3). This would seem to indicate that the data are over fitted. However, as noted above, it may be an indication that the error estimates in the picked travel times are too conservative. A model recovery test (Fig. 13a), for which the model to be recovered was the upper crust of model 1 (Fig. 11a), shows that the main basin structure can be recovered to a depth of about 7–8 km, but that the recovered basin structure is somewhat wider than the input structure at greater depths. The shot and receiver geometry for the recovery test was the same as in the actual experiment and random noise with a standard deviation of 0.06 s was added to the travel times before inversion. This value is similar to the root mean square travel-time residual achieved by the inversion (Table 3). Checkerboard tests with anomalies greater than 10 × 4 km show that the anomalies can be well retrieved horizontally and down to a depth of about 7–8 km. For anomalies of the size 5 × 2 km (Fig. 13b), the anomalies can be quite well retrieved horizontally and down to a depth of about 4 km. For these anomalies, horizontal resolution is better in the eastern part of the profile than in the western part. In order so that model 2 can be better compared to model 1, the model resolution for the upper crust of model 2 is not shown but is very similar to that for the recovery test, which is shown (Fig. 13a).

The main feature obtained in this model is the low-velocity DSB. The low velocities of 4.0–5.0 km s^{-1} for the DSB extend down to about 7–8 km after which resolution is poor (cf. Fig. 13a). The DSB is about 19 km wide at about 5 km depth, although as the model recovery test shows, this width is probably somewhat overestimated at this and greater depths. This model also shows a general deepening of the top of the seismic basement, marked approximately by the colour change from blue to green at a velocity of around 5.7 km s^{-1}, away from the DSB on both sides, but especially on the east side. Inversions using other initial models, including some with additional flattening and/or smoothing, produced end models very similar to that shown here. However, all of these end models had a larger range of velocities except for the end model for which the inverse problem had a grid size of 4 × 2 km. On the other hand, the end model for which the inverse problem had a grid size of 4 × 2 km had a slightly more ragged appearance along the top of the seismic basement, which is marked approximately by the colour change from blue to green at a velocity of around 5.7 km s^{-1}.

Mid-crustal, lower crustal and crust–mantle (Moho) boundaries

First, the depths of the boundary between the upper and lower crust in models 1 and 2 were determined by inverting the 110 travel-time readings of the *Pi2P* reflection (Table 1). Subsequently, the depths to the boundary within the lower crust and the crust–mantle boundary (Moho) in both models were determined. For the lower crustal boundary the 128 travel-time readings for the *Pi3P* reflection were utilized, while for the Moho, the 253 travel-time readings for the *PmP* reflection were used (Table 1). The initial model

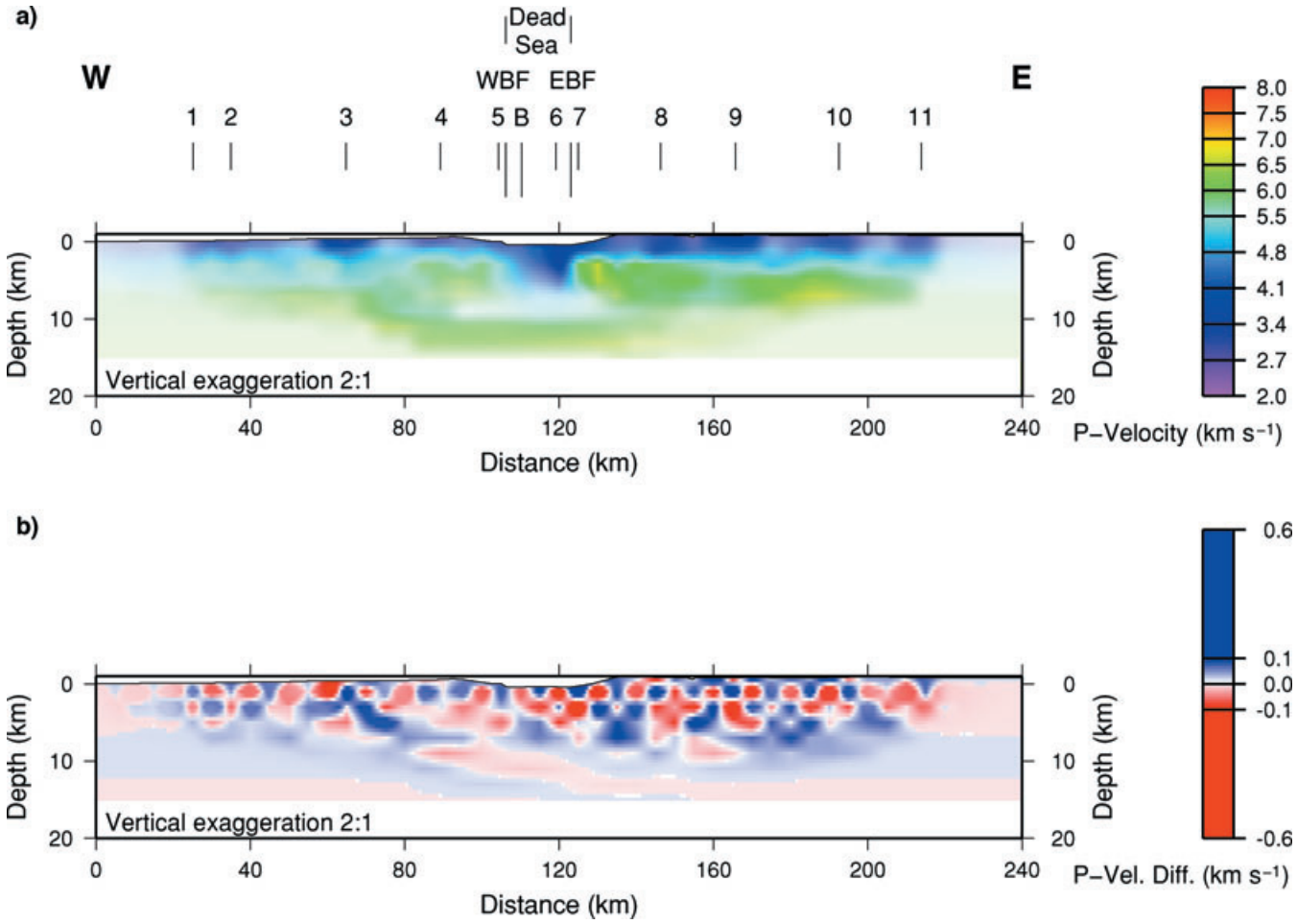

Figure 13. (a) Model recovery test, for which the input travel-time data for the inversion were derived by ray-tracing through the model shown in Fig. 11a. Brighter regions in the model have good ray coverage and are well resolved while fainter regions in the model have poor ray coverage and are poorly resolved. The ray coverage and resolution for the upper crust above 20 km depth of the model shown in Fig. 11b is very similar to that for the model shown in this figure. (b) Checker-board test, for which the input travel-time data for the inversion were derived by ray-tracing through a 5 × 2 km checker-board model with ±0.3 km s^{-1} velocity anomalies. The positions of the shotpoints are marked above the 2-D models. *Key:* see Fig. 10.

consisted of a horizontal boundary at about 20 km depth in the case of the mid-crustal boundary, 27 km in the case of the lower crustal boundary and 32 km in the case of the Moho. During the inversion for the lower crustal boundary, the velocities in the upper part of the lower crust were held fixed at 6.8 km s^{-1} in model 1 and 6.7 km s^{-1} in model 2 as, in the inversion, there is a trade-off between the average velocity of the upper part of the lower crust and the average structure of the lower crustal boundary. A value of 6.7 or 6.8 km s^{-1} for the average velocity of the upper part of the lower crust was chosen based on forward modelling of the amplitudes (Fig. 14) and previous studies in the area (Ginzburg *et al.* 1979a; El-Isa *et al.* 1987a; Weber *et al.* 2004). As there is a similar trade-off between average velocity and depth, during the inversion for the Moho depths, the velocities in the lower part of the lower crust were held fixed at 7.2 km s^{-1}, again based on forward modelling of the amplitudes (Fig. 14). Utilizing the velocities shown in the models ensures that the relative amplitudes of the reflections *Pi2P*, *Pi3P* and *PmP* with respect to one another are qualitatively correct, as can be seen from a comparison with the observed data (Figs 5a and b). A velocity of 7.1 km s^{-1} for the lower layer of the lower crust, for example, produces amplitudes for the *Pi3P* reflection, which are too weak with respect to those of the other reflections.

For each boundary, two or three independent nodes, each with an *a priori* uncertainty of 5 km, were used for models 1 and 2 in the inversions (Tables 2 and 3). Two to four iterations were required in each inversion in order to reduce the average absolute travel-time residuals to the point where no further improvement occurred (Table 3). As above, those χ^2 values, which are below 1 may indicate that the error estimates in the picked travel times are too conservative. The three interfaces are constrained between profile km 70 and 120 (Figs 12c and e) with, in addition, the mid-crustal boundary and the Moho being constrained out to profile km 160 in the east and the mid-crustal and lower crustal boundaries being constrained from profile km 50 in the west. For the lower crustal boundary, as there is no coverage to the east of the DSB, there is not a third independent boundary node to the east of the DSB. In both models 1 and 2, all nodes are well resolved and all off-diagonal elements of the resolution matrix are small compared to the diagonal elements.

Following the final inversion step the boundaries were made to shallow, outside the region of ray coverage, toward the western end of the profile, such that the depth to the mid-crustal boundary and the Moho beneath shotpoint 1, where the DESIRE and DESERT profiles cross, is the same as that below the DESERT profile (Weber *et al.* 2004). Thus, in model 1 the mid-crustal boundary deepens from about 18.5 km depth beneath the western end of the profile

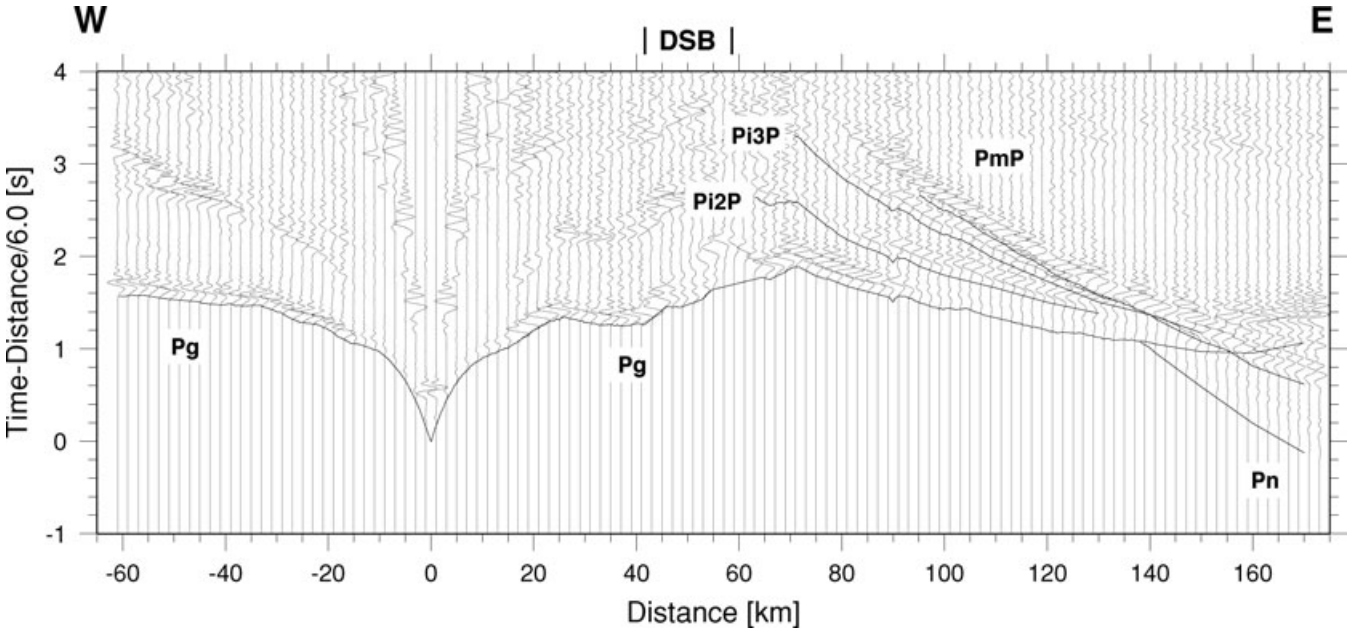

Figure 14. Synthetic seismogram section, calculated with the finite-differences method for shot 3 along the DESIRE wide-angle reflection/refraction (WRR) profile. The observed data for shot 3 are shown in Figs 5a and b. The record section reduced with a velocity of 6 km s^{-1} shows the vertical component of *P*-wave motion in which each trace is normalized individually. Continuous lines represent phases calculated from the model shown in Fig. 11b. The position of the DSB is marked. *Key:* see Fig. 4.

to about 22 km depth beneath profile km 85 and then shallows by about 1.5 km beneath the DSB before deepening to about 22 km depth east of the DSB (Fig. 11a). In model 2, the topography on the mid-crustal boundary is less than in model 1 and the boundary remains at 20.5–21 km depth east of profile km 70 (Fig. 11b). As the two models illustrate quite well, the amount of structure on the boundary depends on the velocity structure above the boundary. The topography on the boundary within the region of ray coverage in models 1 and 2, produces variances for the travel-time residuals which are not, according to the *F* test, significantly different at the 95% confidence limit from those for a model with a flat boundary at about 21.5 km depth in the case of model 1 and about 20.7 km depth in the case of model 2. The lower crustal boundary in model 1 deepens from about 22.5 km depth beneath the western end of the profile to about 26 km depth beneath profile km 80 and then to about 27 km just beneath the western boundary of the DSB (Fig. 11a). In model 2, the topography on this boundary is just slightly greater than, but still very similar to that in model 1 (Fig. 11b). The Moho in model 1 deepens from about 25 km depth beneath the western end of the profile to about 35 km depth beneath profile km 70. It then shallows by about 3 km beneath the DSB, before deepening slightly to about 32.5 km depth east of the DSB (Fig. 11a). In model 2, the topography on the Moho is very similar to that in model 1, but the whole structure is about 0.5–1.0 km shallower in model 2 east of profile km 50 (Fig. 11b). The topography on the Moho within the region of ray coverage in both models, produces variances for the travel-time residuals which can be shown with the *F* test to be significantly different at the 95% confidence limit from those for a model with a flat boundary at about 33.1 km depth in the case of model 1 and about 32.3 km depth in the case of model 2. Apart from one picked arrival on the record section from shot 3 at about 150 km distance range, the Pn phase was not observed, probably due to a lack of energy from the borehole shots beyond about 150 km distance. A velocity of 7.9 km s^{-1} has been assigned to the uppermost mantle based on previous experiments in which the *Pn* phase was observed almost exclusively from water shots and the *Pn* velocity ranged from 7.8 to 8.0 km s^{-1} (Ginzburg et al. 1979a; El-Isa 1987a).

Other initial models for the mid-crustal boundary and the Moho have also been tested. As there is negligible topography on the lower crustal boundary as the DSB is crossed, it was not felt necessary to test other initial models for this boundary. For the mid-crustal boundary and the Moho, initial models with the boundary nodes shifted by 10 km produce, after inversion, very similar end models to those shown here. Models with a shallowing of the mid-crustal boundary of more than 1 km beneath the DSB, produce variances for the travel-time residuals which can be shown with the *F* test to be significantly different at the 95% confidence limit to that for model 2. In contrast, a deepening of this boundary, up to 5 km, beneath the DSB can not be resolved. Models with a shallowing of the Moho of more than 3 km or a deepening of the Moho of more than 2 km beneath the DSB, produce variances for the travel-time residuals which can be shown with the *F* test to be significantly different at the 95% confidence limit to that for a flat boundary at 32.3 km depth. Further, models with dips for the mid-crustal boundary or the Moho similar to those for these boundaries in the model for the USGS profile (ten Brink *et al.* 2006) were also tested. However, the best-fitting models with such dips for either the mid-crustal boundary or the Moho produce a variance for the travel-time residuals which can be shown with the *F* test to be significantly different at the 95% confidence limit to those for either model 1 or model 2. In previous studies in this region, the lower crust has been shown as having one layer, with or without a crust–mantle transition zone beneath, in the seismic models (Ginzburg *et al.* 1979a, b; El-Isa *et al.* 1987a; Weber *et al.* 2004; ten Brink *et al.* 2006), although Weber *et al.* (2004) did consider the possibility of the lower crust comprising two layers beneath at least part of the DESERT profile. To examine the effect of not including the *Pi3P* reflection in the modelling, the depths of the Moho assuming that the velocity in the entire lower crust is 6.8 km s^{-1} in the case of model 1 and 6.7 km s^{-1} in the case

of model 2 are shown (dashed lines in Figs 11a and b). The effect is to cause the Moho depths to decrease by up to 2.6 km, and for the Moho depths to be 3–4 km smaller beneath the DSB than beneath the adjacent flanks of the basin.

DISCUSSION AND SUMMARY

A comparison is shown for depths to the seismic basement, depths to the boundary between the upper and lower crust and depths to the Moho between the DESIRE profile and other seismic profiles, which cross the DESIRE profile (Figs 12a, c and e). In addition, the depth to the top of the Precambrian in the Zohar-8 deep borehole at profile km 93 is shown (Fig. 12a). In the borehole the top of the Precambrian was located at 2 546 m below sea level and the hole penetrated 121 m of the Zenifim formation, consisting of extrusive igneous and arkosic rocks, before bottoming at 2 667 m below sea level (Gilboa *et al.* 1993). In model 1, the depth to the top of the seismic basement beneath the profile at profile km 93 is 2500 m below sea level. Thus, if the seismic basement does represent Precambrian intrusive igneous or metamorphic basement, then the Zenifim formation should be rather thin in this area. West of the DSB the maximum difference in depths to the seismic basement between the DESIRE and other profiles is 1.7 km at profile km 69. The difference between the DESIRE and DESERT profiles where they cross each other at profile km 25 is 1.3 km. East of the DSB the difference in depths to the seismic basement between the DESIRE profile and profile 1 (E1 in Fig. 1) of the 1984 experiment in Jordan (El-Isa *et al.* 1987a) is 0.5 km. Beneath the DSB itself the difference in depths to the seismic basement between the DESIRE profile and profile 2 (W2 in Fig. 1) of the 1977 experiment in Israel (Ginzburg *et al.* 1979a) is 7 km. This is probably because although the shotpoints for this profile were in the DSB and the Gulf of Aqaba/Elat, the recording stations were generally placed along the side of the DSB and the Araba valley. The difference in depths to the seismic basement between the DESIRE profile and a N–S trending profile (DSP in Fig. 1) just west of the axis of the DSB (Ginzburg & Ben-Avraham 1997) is only 2 km. With respect to depths to the boundary between the upper and lower crust (Fig. 12c), the maximum difference between the DESIRE profile and other profiles is 5.8 km at profile km 70 where the USGS profile (ten Brink *et al.* 2006) crosses the DESIRE profile. However, a model with a shape for this boundary similar to that derived from the USGS profile data provides a significantly poorer fit to the DESIRE profile data than the models shown here (Fig. 11), according to the *F* test at the 95% confidence level. With respect to depths to the Moho (Fig. 12e), the maximum difference between the DESIRE profile and other profiles is 6.5 km at profile kms 69 and 70 where profile 6 (W6 in Fig. 1) of the 1977 experiment in Israel (Ginzburg *et al.* 1979a) and the USGS profile (ten Brink *et al.* 2006) cross the DESIRE profile. However, again a model with a shape for the Moho similar to that derived from the USGS profile data provides a significantly poorer fit to the DESIRE profile data than the models shown here (Fig. 11), according to the *F* test at the 95% confidence level.

Beneath the cover which consists of three layers on the western flank of and within the DSB and two layers on the eastern flank of the DSB, the upper crust is divided into two layers as is also the lower crust. Previous studies generally just recognized one layer within both the upper and lower crust (Ginzburg *et al.* 1979a; El-Isa *et al.* 1987a). However, Weber *et al.* (2004) did note the possibility of the lower crust beneath the DESERT profile comprising two layers and Mohsen *et al.* (2005) also found a high-velocity lower crustal layer mainly east of the DST. The top of the seismic basement with velocities of 5.8–6.1 km s^{-1} (Fig. 11a) probably correlates with the top of the Precambrian intrusive igneous or metamorphic rocks. In southwest Jordan where such rocks are exposed at the surface they comprise mainly granites and granodiorites and have velocities close to 6 km s^{-1} (El-Isa *et al.* 1987a). Xenoliths from the lower crust have been found in Cenozoic basalts in northeast Jordan (Nasir 1995). These xenoliths fall into two main types, namely plagioclase-rich mafic granulites and pyroxene-rich mafic granulites. For these xenoliths, velocities have been calculated for lower crustal conditions beneath the region using the method of Sobolev & Babeyko (1994). The upper layer of the lower crust with velocities of 6.7–6.8 km s^{-1} matches the velocities found for the plagioclase-rich mafic granulites while the lower layer with velocities of about 7.2 km s^{-1} matches the velocities found for the pyroxene-rich mafic granulites (Förster *et al*. 2009). Within the cover the depth to the top of the third top layer west of the DSB (Fig. 11a) correlates well with the depth to the top of the Zohar formation of Middle Jurassic age in the Zohar-8 deep borehole (Gilboa *et al.* 1993). In this borehole, above the Zohar formation, sandstone and shale are the dominant lithologies, whereas the top of the Zohar formation marks the point below which limestone is prominent. In the Helez-Deep-1A borehole the period of time represented by the Zohar formation is absent. However, the unconformity between the Lower Cretaceous and Middle Jurassic occurs at 1 858 m depth. A similar depth to the top of the third top layer west of the DSB occurs beneath profile km 50 (Fig. 11a). Thus it may be possible to correlate the top of the third top layer west of the DSB with approximately the top of the Middle Jurassic. East of the DSB the top layer has thicknesses of 1–2 km (Fig. 11a), except close to the DSB where the thickness decreases to just a few hundred metres. As noted above, around shotpoint 7, the thickness of the Mesozoic succession overlying the rocks of Cambrian age is only a few hundred metres. This, in turn, means that around shotpoint 7 the top of the second top layer can be correlated with the unconformity between the Mesozoic and Palaeozoic rocks. Further east, where the DESIRE profile intersects profile 1 (E1 in Fig. 1) of the 1984 experiment (El-Isa *et al.* 1987a), just east of shotpoint 9 (Fig. 1), the top layer in model 1 has a thickness of 1.1 km (Fig. 11a) while the top layer in the model for profile 1 of the 1984 experiment has a thickness of 1.5 km. El-Isa *et al.* (1987a) correlated the top layer in the model for profile 1 of the 1984 experiment with the Tertiary-Mesozoic succession based on the thickness of this layer being in agreement with geological estimates of the thickness of the Tertiary-Mesozoic succession (Bender 1975). In the Swaqa-1 borehole, about 37 km east of the east end of the WRR profile, the unconformity between rocks of Cretaceous age and rocks of Silurian age occurs at 1 325 m depth. Thus, it is attractive to think that all along the WRR profile, the top layer east of the DSB can be correlated with the Tertiary-Mesozoic succession and the second top layer can be correlated with the Palaeozoic succession and rocks of Precambrian age, for example the Saramuj formation, above the Precambrian intrusive igneous and metamorphic basement.

With the completion of the DESIRE profile there are now three modern WRR profiles crossing the DST. Based on the results from these three profiles, two N–S sections have been constructed (Fig. 15), one along the axis of the DSB and further south, the Araba valley and one 20 km east of the structure on the eastern flank. The two sections show that there is very little E–W variation in depths to the Moho and the top of the lower crust. They also show that the N–S variations in depths to the Moho and the top of the lower crust are very similar between the two sections. The main difference is

in the N–S variation in the thickness of the upper crust in going from south to north. Beneath the DESERT profile in the south the upper crust, including the pre-DST sediments, is about 18 km thick beneath the Araba valley. Further north beneath the DSB, the upper crust thins to 11–12 km beneath the USGS and DESIRE profiles. In contrast, 20 km east of the structure on the eastern flank the thickness of the upper crust remains more or less constant at 20–22 km. It is thus thought that the Dead Sea pull-apart basin is essentially an upper crustal feature with upper crustal extension (Fig. 2g) associated with the left-lateral motion along the DST (Fig. 2b) and the side-stepping of the major strike-slip motion from the east side of the valley at the southern end of the basin to the west side of the valley north of the basin. The boundary between the upper and lower crust at about 20 km depth might act as a decoupling zone. Below this boundary the two plates move past each other in what is essentially a shearing motion. Within the upper mantle this zone is about 20 km wide based on a study of seismic anisotropy using SKS waves (Rümpker *et al.* 2003; Ryberg *et al.* 2005).

The N–S sections (Fig. 15) have been drawn without taking into account the left-lateral movement along the DST. The DESIRE WRR profile crosses the DST about 95 km north of where the DESERT WRR profile crossed the DST. If the 107 km of left-lateral movement is removed, then the structure beneath the DESIRE WRR profile east of the DST should only have been 12 km south of the structure beneath the DESERT WRR profile west of the DST, before movement along the DST started. Neglecting the 12 km difference,

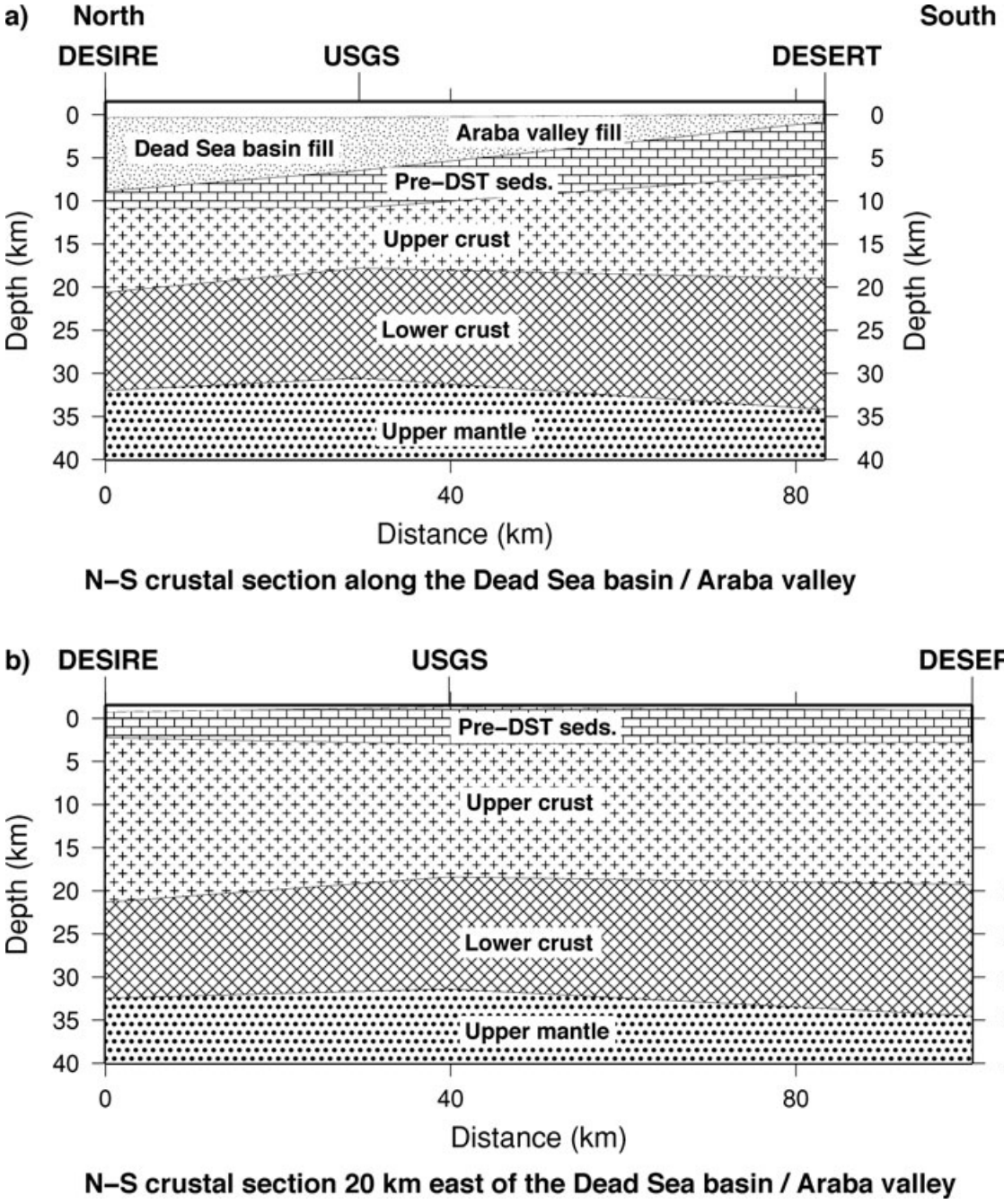

Figure 15. (a) N–S section along the DSB/Araba valley. (b) N–S section 20 km east of the DSB/Araba valley. *Key*: Pre-DST seds—sediments deposited prior to the formation of the DST.

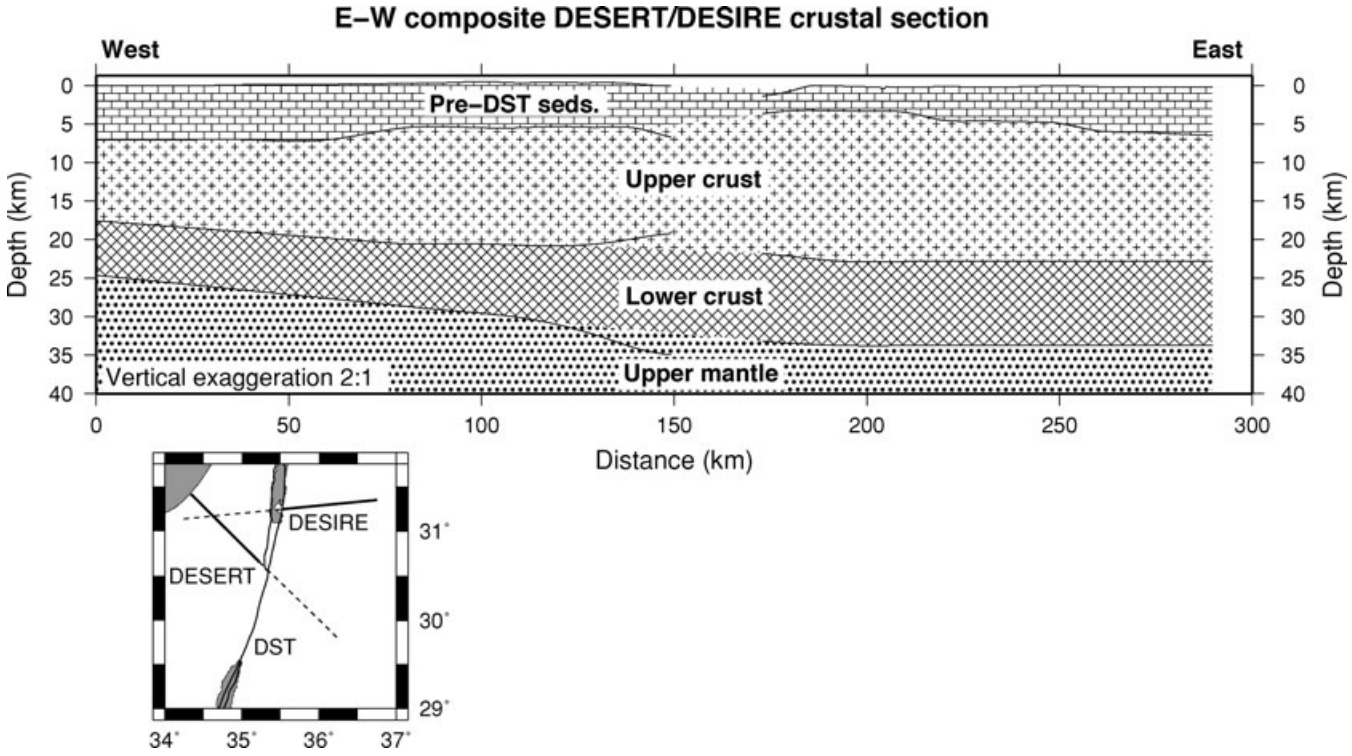

Figure 16. E–W composite crustal section using the main interfaces from the final model of the DESERT WRR profile west of the DST and from model 1 (Fig. 11a) of the DESIRE WRR profile east of the DST, thus restoring the 107 km of left-lateral movement along the DST. In the inset map, the parts of the profiles used to construct the cross-section are shown as thick black lines. *Key:* see Fig. 15.

a composite cross-section incorporating the main crustal interfaces from the final model of the DESERT WRR profile west of the DST and from model 1 (Fig. 11a) of the DESIRE WRR profile east of the DST has been constructed (Fig. 16). In constructing this cross-section 1 km of uplift of the eastern side of the DST has also been removed and the structure beneath the approximately 20 km wide Araba valley has been omitted. The pattern boundaries in the gap show one possibility of how the structure might have looked before the start of formation of the DST. If this configuration is correct, then it provides additional evidence for the hypothesis (Steckler & ten Brink 1986; El-Isa *et al.* 1987a) that the DST formed at the point where the crust starts to thin toward the Mediterranean Sea. In this hypothesis, based originally on an idea by Vink *et al.* (1984), the transform will preferentially form in the thicker, weaker crust at the western edge of the Nubo-Arabian shield than in the thinner, stronger crust in the vicinity of the Mediterranean Sea. It is interesting to note that at the same point there is a thickening of the sediments deposited prior to the formation of the DST toward the west (Fig. 16).

Based on the model for the USGS profile, ten Brink *et al.* (2006) provided some possible explanations for the formation of the DSB being essentially confined to the upper crust. Thermo-mechanical modelling of the DSB (Sobolev *et al.* 2005; Petrunin & Sobolev 2006) also supports a scenario of the DSB being essentially an upper crustal feature with little involvement of the lower crust and the Moho. In particular, Petrunin & Sobolev (2006) predicted that not more than 3 km of Moho uplift occurs beneath the DSB (Fig. 2g). This prediction is confirmed by the present study especially on the eastern side of the DSB where there is not more than 1 km of topography on the Moho as one goes from the basin to the flank. The small depression in the Moho under the western flank of the basin may be a pre-existent feature and may be a feature which is present all along the western flank of the DSB and Araba valley. Such a feature was recognized beneath the DESERT profile (Weber *et al.* 2004) where it coincides spatially with the 20 km wide anisotropic zone related to the DST in the upper mantle (Rümpker *et al.* 2003; Ryberg *et al.* 2005). It was also recognized further south near the northern end of the Gulf of Aqaba/Elat on profile 5 (W5 in Fig. 1) of the experiment carried out on the western side of the DST in 1977 (Ginzburg *et al.* 1979a). However, it was not recognized beneath the USGS profile (Ten Brink *et al.* 2006). One of the open questions still remaining is to what extent this feature really does exist and how does it relate to the DST.

A further feature of the modelling of Petrunin & Sobolev (2006) is that N–S extension is the main cause for the thinning of the upper crust beneath the DSB and E–W extension is only a very minor component. The N–S sections shown here (Fig. 15) based on the DESERT, USGS and DESIRE WRR seismic profiles crossing the DST, are compatible with the modelling of Petrunin & Sobolev (2006). However, the models for the DESIRE WRR profile (Fig. 11) are compatible with models involving N–S and/or E–W extension. In this respect, the few focal mechanisms that exist, for earthquakes in the DSB, show extension both parallel and perpendicular to the trend of the basin in addition to the dominant strike-slip motion (van Eck & Hofstetter 1989, 1990).

In summary, models of the *P*-wave velocity structure derived from the data from the DESIRE wide-angle reflection/refraction (WRR) profile show that the sedimentary infill associated with the formation of the southern DSB is about 8.5 km thick beneath the profile. With around an additional 2 km of older sediments, the depth to the seismic basement beneath the southern DSB is about 11 km below sea level beneath the profile. From the N–S trending profile along the Dead Sea, there is evidence that the seismic basement continues to deepen to a maximum depth of about 14 km, about

10 km south of the DESIRE profile (Ginzburg & Ben-Avraham 1997). In contrast, the interfaces below about 20 km depth, including the top of the lower crust and the Moho, probably show less than 3 km variation in depth beneath the profile as it crosses the southern DSB. Thus the Dead Sea pull-apart basin may be essentially an upper crustal feature with upper crustal extension (Fig. 2g) associated with the left-lateral motion along the Dead Sea Transform (Fig. 2b). The boundary between the upper and lower crust at about 20 km depth might act as a decoupling zone. Below this boundary the Arabian and African plates move past each other in what is essentially a shearing motion.

ACKNOWLEDGMENTS

The DESIRE project was funded by the Deutsche Forschungsgemeinschaft. The National Ministry of Infrastructure of Israel, the Natural Resources Authority of Jordan and the An-Najah National University in Nablus, Palestine are thanked for their support. Our contractors the Geophysical Institute of Israel and the Chemical and Mining Industries (Jordan) are thanked for their excellent work under difficult logistic conditions. The cooperation of the Dead Sea Works Ltd. in Israel and the Arab Potash Company in Jordan in allowing the DESIRE project to work in their properties is gratefully acknowledged. The instruments used in the field program were provided by the Geophysical Instrument Pool of the Deutsches GeoForschungsZentrum—GFZ, and the PASSCAL facility of the Incorporated Research Institutions for Seismology (IRIS) through the PASSCAL Instrument Center at New Mexico Tech. Data collected during this experiment with the PASSCAL instruments are available through the IRIS Data Management Center. The facilities of the IRIS Consortium are supported by the National Science Foundation under Cooperative Agreement EAR-0004370 and by the Department of Energy National Nuclear Security Administration. The following persons are acknowledged for their participation in the fieldwork of the seismic wide-angle reflection/refraction experiment—W. Abdelhafez, B. Al-Biss, A. Al-Massri, H. Al-Rashdan, M. Amberger, A. Arbel, N. Attiyat, J. Bartlakowski, K. Bauer, R. Ben-Ari, B. Braeuer, L. Carothers, C. Ehlert, O. Gaede, J.-A. Gueldner, G. Haim, M. Hatamleh, M. Harahsheh, M. Hasan, M. Hijazi, N. Jahid, D. Jaser, S. Jetschny, J. Khataibeh, E. Korger, F. Kretschmer, M. Meiler, M. Mieth, M. Milkawi, P. Miller, S. Muneizel, M. Paschke, K. Razeq, A. Rohrmann, M. Rumpf, T. Sawaqi, A. Schulze, A. Siebert, F. Stier, M. Stiller, G. Swidan, T. Talat, M. Wahle, S. Wenk and M.-K. Yoon. M. Paschke helped with the data processing and model calculations.

REFERENCES

Al-Zoubi, A. & ten Brink, U., 2002. Lower crustal flow and the role of shear in basin subsidence: an example from the Dead Sea basin, *Earth Planet. Sci. Lett.,* **199,** 67–79.

Bartov, Y., 1990. Geological photomap of Israel and adjacent areas, *The Survey of Israel,* Tel Aviv.

Ben-Avraham, Z. & Zoback, M.D., 1992. Transform-normal extension and asymmetric basins: an alternative to pull-apart models, *Geology,* **20,** 423–426.

Ben-Avraham, Z., Ginzburg, A., Makris, J. & Eppelbaum, L., 2002. Crustal structure of the Levant Basin, eastern Mediterranean, *Tectonophysics,* **346,** 23–43.

Ben-Avraham, Z. & Schubert, G., 2006. Deep 'drop down' basin in the southern Dead Sea, *Earth Planet. Sci. Lett.,* **251,** 254–263, doi: 10.1016/j.epsl.2006.09.008.

Bender, F., 1975. Geology of the Arabian Peninsula, Jordan. *U.S. Geol. Surv., Prof. Pap.,* **560-I,** 36 pp.

Červený, V., Molotkov, I.A. & Pšenčík, I., 1977. *Ray Method in Seismology*, University of Karlova, Prague.

El-Isa, Z., Mechie, J., Prodehl, C., Makris, J. & Rihm, R., 1987a. A crustal structure study of Jordan derived from seismic refraction data, *Tectonophysics,* **138,** 235–253.

El-Isa, Z., Mechie, J. & Prodehl, C., 1987b. Shear velocity structure of Jordan from explosion seismic data, *Geophys. J.R. astr. Soc.,* **90,** 265–281.

Freund, R., Garfunkel, Z., Zak, I., Goldberg, M., Weissbrod, T. & Derin, B., 1970. The shear along the Dead Sea rift, *Phil. Trans. R. Soc. Lond., A,* **267,** 107–130.

Förster, H.-J., Förster, A., Oberhänsli, R. & Stromeyer, D., 2009. Lithospheric composition and thermal structure of the Arabian Shield in Jordan. *Tectonophysics*, doi: 10.1016/j.tecto.2008.11.014.

Fuchs, K. & Müller, G., 1971. Computation of synthetic seismograms with the reflectivity method and comparison with observations, *Geophys. J.R. astr. Soc.,* **23,** 417–433.

Fuis, G.S., Mooney, W.D., Healy, J.H., McMechan, G.A. & Lutter, W.J., 1984. A seismic refraction survey of the Imperial Valley region, California. *J. Geophys. Res.,* **89,** 1165–1189.

Garfunkel, Z., 1981. Internal structure of the Dead Sea leaky transform (rift) in relation to plate kinematics, *Tectonophysics,* **80,** 81–108.

Garfunkel, Z., 1997. The history and formation of the Dead Sea basin, in *The Dead Sea—The Lake and its Setting*, pp. 36–56, eds Niemi, T.M., Ben-Avraham, Z. & Gat, J.R. *Oxford Monographs on Geology and Geophysics*, No. 36, Oxford University Press, Oxford.

Garfunkel, Z. & Ben−Avraham, Z., 1996. The structure of the Dead Sea basin, *Tectonophysics,* **266,** 155–176.

Gilboa, Y., Fligelman, H. & Derin, B., 1993. Zohar–Kidod–Haqanaim fields—Israel, Eastern Mediterranean Basin, in *Treatise of petroleum geology atlas of oil and gas fields*, pp. 129–152, eds N.H. Foster and E.A. Beaumont, *Am. Assoc. of Pet. Geol.*, Tulsa, Oklahoma.

Ginzburg, A., Makris, J., Fuchs, K., Prodehl, C., Kaminski, W. & Amitai, U., 1979a. A seismic study of the crust and upper mantle of the Jordan-Dead Sea Rift and their transition toward the Mediterranean Sea, *J. Geophys. Res.,* **84,** 1569–1582.

Ginzburg, A., Makris, J., Fuchs, K., Perathoner, B. & Prodehl, C., 1979b. Detailed structure of the crust and upper mantle along the Jordan-Dead Sea Rift, *J. Geophys. Res.,* **84,** 5605–5612.

Ginzburg, A. & Ben-Avraham, Z., 1997. A seismic refraction study of the north basin of the Dead Sea, Israel, *Geophys. Res. Lett.,* **24,** 2063–2066.

Kashai, E.L. & Croker, P.F., 1987. Structural geometry and evolution of the Dead Sea—Jordan rift system as deduced from new subsurface data, *Tectonophysics,* **141,** 33–60.

Kelly, K.R., Ward, R.W., Treitel, S. & Alford R.M., 1976. Synthetic seismograms: a finite difference approach, *Geophysics,* **41,** 2–27.

Lutter, W.J. & Nowack, R.L., 1990. Inversion for crustal structure using reflections from the PASSCAL Ouachita experiment, *J. Geophys. Res.,* **95,** 4633–4646.

Lutter, W.J., Nowack, R.L. & Braile, L.W., 1990. Seismic imaging of upper crustal structure using travel times from the PASSCAL Ouachita experiment, *J. Geophys. Res.,* **95,** 4621–4631.

Makris, J., Ben-Avraham, Z., Behle, A., Ginzburg, A., Giese, P., Steinmetz, L., Whitmarsh, R.B. & Eleftheriou, S., 1983. Seismic refraction profiles between Cyprus and Israel and their interpretation, *Geophys. J. R. astr. Soc.,* **75,** 575–591.

Mechie, J., Abu-Ayyash, K., Ben-Avraham, Z., El-Kelani, R., Mohsen, A., Rümpker, G., Saul, J. & Weber, M., 2005. Crustal shear velocity structure across the Dead Sea Transform from 2-D modelling of project DESERT explosion seismic data, *Geophys. J. Int.,* **160,** 910–924, doi: 10.1111/j.1365–246X.2005.02526.x.

Mohsen, A., Hofstetter, R., Bock, G., Kind, R., Weber, M., Wylegalla, K., Rümpker, G. & the DESERT Group, 2005. A receiver function study across the Dead Sea Transform, *Geophys. J. Int.,* **160,** 948–960, doi: 10.1111/j.1365–246X.2005.02534.x.

Nasir, S., 1995. Mafic lower crustal xenoliths from the northwestern part of the Arabian Plate, *Eur. J. Mineral.,* **7,** 217–230.

Nolet, G., 1987. Seismic wave propagation and seismic tomography, in *Seismic Tomography*, pp. 1–24, ed G. Nolet, D. Reidel, Norwell, Massachusetts, USA.

Quennell, A.M., 1958. The structural geomorphic evolution of the Dead Sea Rift, *Quart. J. Geol. Soc. London,* **114,** 1–24.

Paige, C.C. & Saunders, M.A., 1982. LSQR: an algorithm for sparse linear equations and sparse least squares. *Assoc. Comput. Mach. Trans. Math. Software,* **8,** 43–71.

Petrunin, A. & Sobolev, S.V., 2006. What controls thickness of sediments and lithospheric deformation at a pull-apart basin? *Geology,* **34,** 389–392, doi: 10.1130/G22158.1.

Podvin, P. & Lecomte, I., 1991. Finite difference computation of traveltimes in very contrasted velocity models: a massively parallel approach and its associated tools, *Geophys. J. Int.,* **105,** 271–284.

Reynolds, A.C., 1978. Boundary conditions for the numerical solution of wave propagation problems, *Geophysics,* **43,** 1099–1110.

Rümpker, G., Ryberg, T., Bock, G. & Desert Seismology Group, 2003. Boundary-layer mantle flow under the Dead Sea transform fault inferred from seismic anisotropy, *Nature,* **425,** 497–501.

Ryberg, T., Rümpker, G., Haberland, C., Stromeyer, D. & Weber, M., 2005. Simultaneous inversion of shear wave splitting observations from seismic arrays, *J. Geophys. Res.,* **110,** B03301, doi: 10.1029/2004JB003303.

Sandmeier, K.-J., 1990. Untersuchung der Ausbreitungseigenschaften seismischer Wellen in geschichteten und streuenden Medien, *PhD thesis*. Karlsruhe University.

Schneider, W.A., Ranzinger, K.A., Balch, A.H. & Kruse, C., 1992. A dynamic programming approach to first arrival traveltime computation in media with arbitrarily distributed velocities, *Geophysics,* **57,** 39–50.

Sobolev, S.V. & Babeyko, A.Yu., 1994. Modelling of mineralogical composition, density and elastic wave velocities in the unhydrous rocks, *Surv. Geophys.,* **15,** 515–544.

Sobolev, S.V., Petrunin, A., Garfunkel, Z., Babeyko, A.Y. & DESERT Group, 2005. Thermo-mechanical model of the Dead Sea Transform, *Earth planet. Sci. Lett.,* **238,** 75–95, doi: 10.1016/j.epsl.2005.06.058.

Steckler, M.S. & ten Brink, U.S., 1986. Lithospheric strength variations as a control on new plate boundaries: examples from the northern Red Sea region, *Earth Planet. Sci. Lett.,* **79,** 120–132.

ten Brink, U.S., Ben−Avraham, Z., Bell, R.E., Hassouneh, M., Coleman, D.F., Andreasen, G., Tibor, G. & Coakley, B., 1993. Structure of the Dead Sea pull−apart basin from gravity analysis, *J. Geophys. Res.,* **98,** 21877–21894.

ten Brink, U.S., Al-Zoubi, A.S., Flores, C.H., Rotstein, Y., Qabbani, I., Harder, S.H. & Keller, G.R., 2006. Seismic imaging of deep low-velocity zone beneath the Dead Sea basin and transform fault: implications for strain localization and crustal rigidity, *Geophys. Res. Lett.,* **33,** L24314, doi: 10.1029/2006GL027890.

van Eck, T. & Hofstetter, R., 1989. Microearthquake activity in the Dead Sea region. *Geophys. J. Int.,* **99,** 605–620.

van Eck, T. & Hofstetter, R., 1990. Fault geometry and spatial clustering of microearthquakes along the Dead Sea—Jordan rift fault zone. *Tectonophysics,* **180,** 15–27.

Vidale, J., 1988. Finite-difference calculation of travel times, *Bull. Seismol. Soc. America,* **78,** 2062–2076.

Vink, G.E., Morgan, W.J. & Zhao, W.-L., 1984. Preferential rifting of continents: a source of displaced terranes. *J. Geophys. Res.,* **89,** 10072–10076.

Weber, M. et al., 2004. The crustal structure of the Dead Sea Transform, *Geophys. J. Int.,* **156,** 655–681, doi: 10.1111/j.1365–246X.2004.02143.x.

Zelt, C.A. & Smith, R.B., 1992. Seismic traveltime inversion for 2-D crustal velocity structure, *Geophys. J. Int.,* **108,** 16–34.

Zelt, C.A. & Barton, P.J., 1998. Three-dimensional seismic refraction tomography: a comparison of two methods applied to data from the Faeroe Basin, *J. Geophys. Res.,* **103,** 7187–7210.